APPENDIX A

DEVELOPMENT AND VALIDATION OF THE UIUC 24–LAYER ST–GCM

1. Introduction

A GCM that can resolve the stratosphere is in need to calculate the radiation forcing of the Mount Pinatubo volcanic eruption and to simulate the climate changes induced by the eruption. A 24–layer stratosphere/troposphere general–circulation model (ST–GCM) has been developed based on the UIUC 7–layer AGCM (Oh 1989) and the UIUC 11–layer AGCM (Wang 1996). In addition to its use in this study, this model has been used to reconstruct the radiative forcing of historical volcanic eruptions (Andronova *et al.* 1999), been coupled with the UIUC atmospheric chemical transport model (ACTM) in an off–line mode to simulate the distributions of source gases and ozone in the stratosphere (Rozanov *et al.* 1999a,b), and been used to simulate the transient climate with prescribed sea–surface temperature (SST) and sea–ice distributions from 1979 to 1995 for the Second Atmospheric Model Intercomparison Project (Gleckler 1999). These studies proved in part the model's capabilities in simulating climate and climate changes.

We further validate this model by performing a long–term simulation with prescribed present climatological SST and sea–ice distributions, and by comparing the simulated results with observations. We also document the structure and development of this model for future references. Section 2 describes the model's basic structure and its treatments of the unresolved sub–grid–scale physical processes. Section 3 validates the model's performance in simulating the present climate. Section 4 examines the influence of the combined uses of Rayleigh friction and an orographic–type gravity–wave–drag parameterization in a 36–layer troposphere–stratosphere–mesosphere version of the GCM. Section 5 summarizes this appendix.

2. Model Description and Sensitivity Studies

The 24–layer ST–GCM is a descendent of the 2–layer tropospheric GCM developed in the late 1960's and early 1970's by Arakawa and Mintz at UCLA (Gates *et al.* 1971), and subsequently

developed and used by Schlesinger during the past 26 years, first at the Rand Corporation from 1973 to 1976, second at Oregon State University (OSU) from 1976 to 1989 (Ghan *et al.* 1982), and since 1989 at the University of Illinois at Urbana–Champaign. The 2–layer AGCM has been used for many simulation studies, including the onset of the last ice age (Schlesinger and Verbitsky 1996) and the equilibrium climate change induced by doubling the CO_2 concentration (Schlesinger and Zhao 1989) – which has been used in many climate impact analyses, such as that published in 1989 by the U.S. Environmental Protection Agency (Smith and Tirpak 1989), wherein it is known as the OSU model.   Beginning in 1984, Schlesinger and Oh developed a 7–layer version of this tropospheric GCM. The 7–layer AGCM, with its top at 200 hPa, differs from the 2–layer AGCM mainly in its vertical resolution and the treatment of radiation, clouds, precipitation and the planetary boundary layer (Oh 1989). Oh used this model for his Ph.D. study at OSU to develop and test a physically based parameterization of clouds and their radiative interactions (Oh 1989). Wang (1996) developed an 11–layer lower–stratosphere/troposphere GCM by extending the model top of the 7–layer AGCM to 50 hPa and adding a few layers in the lower stratosphere. The 11–layer AGCM possesses the same dynamic and physical features as the 7–layer AGCM, but is significantly improved in simulating the present climate, especially the tropical intraseasonal oscillation (Wang and Schlesinger 1999).

Since 1994, a 24–layer ST–GCM has been under development, primarily based on the 11–layer AGCM. Important changes made to the 24–layer ST–GC model include: (1) new parameterizations of radiative transfer for both the terrestrial and solar radiation; (2) update of the interaction between clouds and radiation; (3) inclusion of the radiative effects of aerosols in both the troposphere and stratosphere; and (4) inclusion of a parameterization for orographically excited subgrid–scale gravity–wave drag. The 24–layer ST–GCM is described below in terms of: (1) its predicted quantities and solution methods, and (2) its parameterizations – the treatment of its unresolved–scale physical processes.

a. **Predicted Quantities and Numerical Solution Methods**

The model prognostically calculates the velocity, temperature, water–vapor mixing ratio and the amounts of water and ice clouds for 24 specified vertical layers in the atmosphere, together with the surface pressure, ground temperature, soil water and snow mass, and diagnostically calculates many other quantities, including the temperature and water–vapor content of the surface air (2 meters above the ground), the cloud droplet number concentration and cloud amount, and the rainfall and snowfall. In the version of the 24–layer ST–GCM coupled to our ACTM with interactive photochemistry, many chemical species are also prognostic variables (Rozanov *et al.* 1999a,b).

The horizontal distribution of dependent variables in the model is staggered according to the B–grid to simulate the process of geostrophic adjustment (Arakawa and Lamb 1977), and the model uses finite differences that conserve the total atmospheric mass, total energy under adiabatic and frictionless motion, and enstrophy for the nondivergent component of the wind field (Arakawa 1966). The model's grid is latitude–longitude, with a 4° by 5° resolution (Fig. A–1).
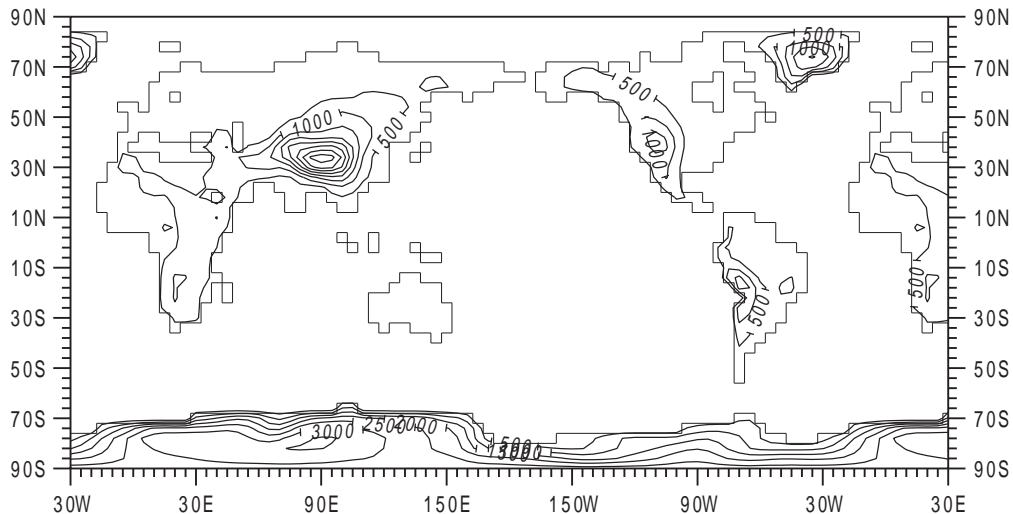

Fig. A–1. *The continental outline and surface elevation (m) of the UIUC 24–layer ST–GCM, with 4° latitude by 5° longitude resolution. The contour interval for the surface elevation is 500 m. The primary grid is centered at latitudes ±2°, ±6°, ... and longitudes 0°, ±5°, ...*

Vertically the model extends from the earth's surface to 1 hPa (Fig. A–2). The model uses sigma (σ) as its vertical coordinate, such that the earth's surface is the coordinate surface $\sigma = 1$ and the top of the model is the coordinate surface $\sigma = 0$. The structure of the vertical layers was chosen to: (1) resolve the peak of the ozone concentration around 10 hPa, (2) eliminate internal wave reflection and overcome computational modes (Tokioka 1978), and (3) represent well the planetary boundary layer. The pressure values at half–integer levels in the first 10 layers in the upper atmosphere follow $p_{k+1/2} = p_{k-1/2}e^d$, where $d = \left(\ln p_{10+1/2} - \ln p_T\right)/10$, $p_T = p_{1/2} = 1$ mb, $p_{10+1/2} \approx 100$ mb, and k enumerates the layers downward from the top layer of the model, k =1, to the 10th layer. There are 14 model layers from about 100 hPa to the earth's surface with preset pressure values for a given surface pressure of 1000 hPa (Fig.2).

The adiabatic and frictionless terms in the primitive equations, and in the conservation equations for water vapor and cloud water/ice, are integrated in time using a sequence of 10 steps per simulated hour, comprised of six time–alternating–space–uncentered (TASU) steps with the Matsuno scheme and four space–centered steps with the leap–frog scheme. The diabatic and frictional terms in these equations are evaluated once per simulated hour. To avoid having to reduce the timestep to maintain linear computational stability in high latitudes where the meridians converge, a longitudinal smoothing of the zonal pressure gradient and the zonal mass flux is performed poleward of 34° latitude. This time integration of the model requires about 75 hours of Cray C–90 computer time per simulated year.

b. Parameterizations – Treatment of Unresolved–Scale Physical Processes

Due to computational constraints, there are many unresolved–scale (subgrid–scale) physical processes whose effects on the resolved–scale quantities are calculated in terms of those quantities alone, that is, they are parameterized. These are described below for: (1) the surface and planetary boundary layer; (2) subgrid–scale transports, convection, large–scale condensation, precipitation and cloud; (3) radiative transfer; (4) aerosols and (5) gravity–wave drag. A more detailed description of parameterizations (1) and (2) is given by *Oh* (1989).
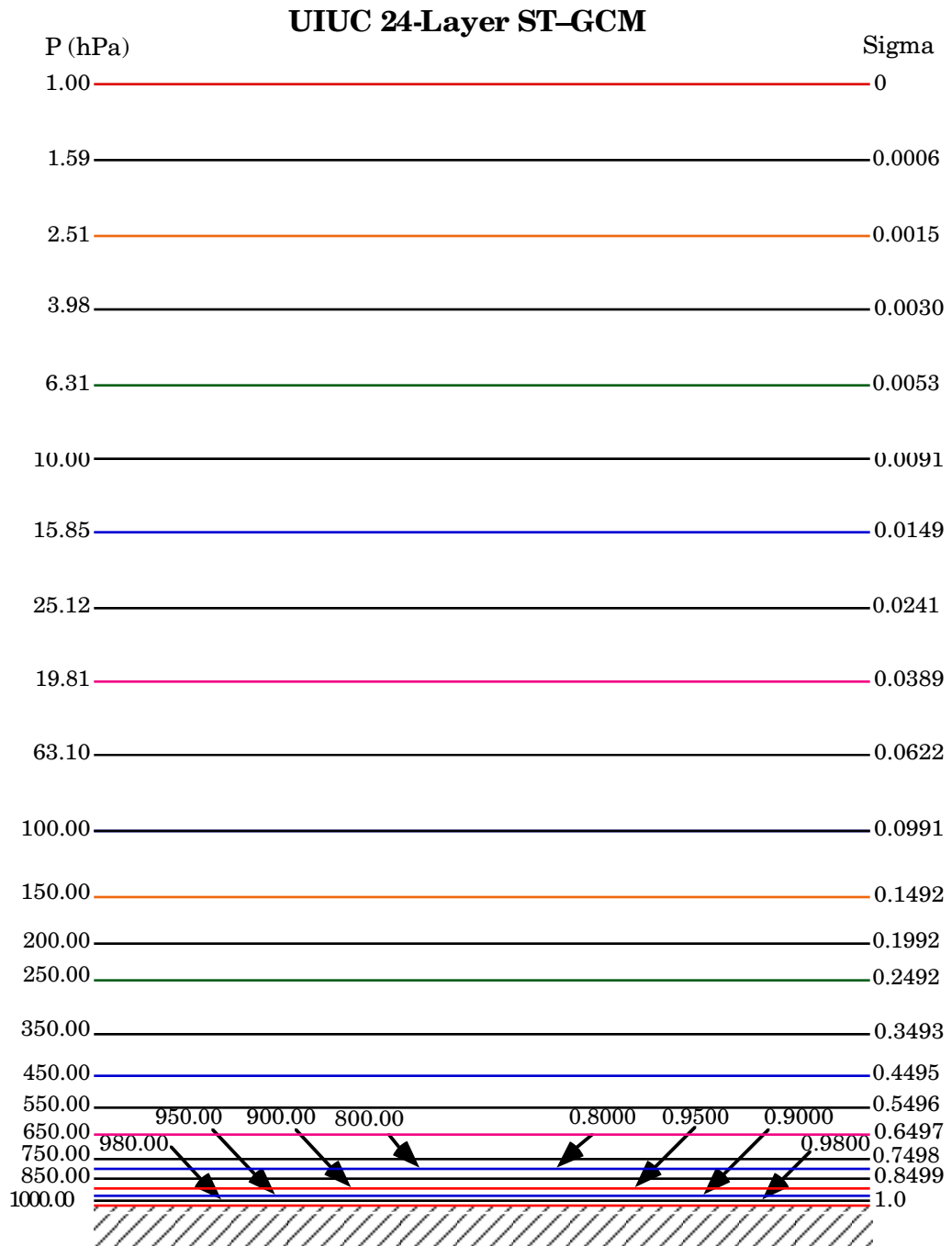
UIUC 24-Layer ST–GCM

P (hPa)   Sigma

P (hPa)	Sigma
1.00	0
1.59	0.0006
2.51	0.0015
3.98	0.0030
6.31	0.0053
10.00	0.0091
15.85	0.0149
25.12	0.0241
19.81	0.0389
63.10	0.0622
100.00	0.0991
150.00	0.1492
200.00	0.1992
250.00	0.2492
350.00	0.3493
450.00	0.4495
550.00	0.5496
650.00	0.6497
750.00	0.7498
850.00	0.8499
1000.00	1.0

950.00   900.00   800.00   0.8000 0.9500 0.9000
980.00   0.9800

Fig. A–2.   *The vertical structure of the UIUC 24–layer ST–GCM.*

(1)   Surface and planetary boundary layer

The topography of the model is that obtained by area–averaging 1°x1° topography (Gates and Nelson 1975) over each of the model's 3312 4°x5° grid cells (Fig. A–1). The surface roughness length over land is taken as the maximum of a function of the standard deviation of the topography (Fiedler and Panofsky 1972) and the roughness length of the local vegetation, including a "zero plane displacement" value for tall vegetation types (Monteith 1973). Over sea ice, the roughness length is constant (Doronin 1969). Over ocean, the roughness is a function of the surface wind speed. In the version of the model in which sea surface temperature and sea ice extent are not calculated, their distributions are prescribed from the AMIP–II climatology. In the version of the model in which sea surface temperature and sea–ice extent are calculated, they are done so by a fixed–depth, 60 meter, mixed–layer ocean model and a thermodynamic sea–ice model.

The turbulent surface fluxes of momentum, sensible heat and moisture are parameterized by bulk formulas that depend on the differences of the momentum, temperature and moisture between the ground and surface air, the surface–air wind speed, and aerodynamic drag and transfer coefficients. The surface–air wind is taken as a fraction of the winds extrapolated from the lowest two model layers. For comparison with observations, sea–level pressure, surface–air temperature, and geopotential height and temperature below ground are diagnosed following Trenberth *et al.* (1993). The surface–air moisture is taken to be the same as that at the lowest atmospheric level (Fig. A–2). The aerodynamic drag and transfer coefficients depend on the vertical stability and surface roughness length, with the same transfer coefficient used for the fluxes of sensible heat and moisture. The surface moisture flux depends on evaportranspiration efficiency, taken as unity over snow, ice and water, and as a function of the soil wetness over land.

The ground temperature is taken to be the average temperature over the diurnal skin depth, calculated from a prognostic budget equation whose source and sink terms include the surface fluxes of radiation, sensible heat and latent heat, and the heat transfer into the ground. The latter depends on the thermal conductivity and bulk heat capacity of the ground.

The soil wetness is determined from a prognostic budget equation that includes the rates of precipitation, snowmelt, surface evaporation and runoff. Soil wetness is the ratio of the soil moisture content to the field capacity, the latter prescribed for each of the 35 combinations of the AGCM's 5 soil textures (sandy; sandy loam; light loam; loamy; and heavy loam, clay) and 7 surface types {(1) evergreen wood and forest; (2) mixed and deciduous wood, and forest; (3) grassland; (4) cropland; (5) shrub and semi–desert; (6) desert; and (7) tundra, mountain, arctic flora)}(Vinnikov and Yeserkepova 1991). The evapotranspiration efficiency over land is taken as the minimum of 4/3 the soil wetness and unity. The runoff rate is a nonlinear function of the soil wetness and the combined rates of precipitation and snowmelt. If the predicted soil wetness exceeds unity, the excess moisture is taken as additional runoff.

The snow mass is determined from a prognostic budget equation that includes the rates of snow accumulation, melting and sublimation. Precipitation falls as snow if the temperature for the lowest model layer is less than 0°C. The snowmelt rate is computed over land from the difference between the downward heat fluxes at the surface and the upward heat fluxes that would occur for a ground temperature equal to the melting temperature of snow (0°C). Snowmelt contributes to the soil moisture. Accumulation and melting of snow may also occur on sea ice. The surface sublimation rate is equated to the evaporative flux from snow, unless sublimation removes all the snow mass in less than one hour, in which case the sublimation rate is set equal to the snow–mass removal rate.

The dependence of the albedo of snow–covered surfaces on solar zenith angle and snow temperature has been included in the model following Briegleb and Ramanathan (1982). The seasonal variation of the albedo of snow–free surfaces is prescribed from the observational data compiled by Matthews (1983). Surface albedo has been made a linear function of the snow–covered and snow–free albedo, weighted by a function of snow depth and surface roughness. The top of the planetary boundary layer (PBL) is taken to be the height of the lowest four atmospheric layers (Fig. A–2). Cloud in the PBL is diagnostically computed on the basis of a cloud–topped mixed–layer model (Guinn and Schubert 1989; Lilly 1968).

(2) **Subgrid–scale transports, convection, large–scale condensation, precipitation and clouds**

The model has parameterized stability–dependent, subgrid–scale turbulent vertical transports of heat, water vapor and horizontal momentum. There are no subgrid–scale turbulent horizontal transports of these quantities. A momentum drag is included in the top layer of the model that is proportional to air density and the square of the velocity (Hansen *et al.* 1983).

The model has three parameterizations for convection: (1) dry–convective adjustment, (2) middle–level convection, and (3) penetrating convection. Dry–convective adjustment occurs if the temperature lapse rate between any two adjacent vertical layers is absolutely unstable, that is, exceeds the dry–adiabatic lapse rate. If this occurs, the instability is instantaneously removed by adjusting the temperatures of the two layers such that their lapse rate is dry adiabatic. This is done by transferring heat vertically between the layers under the constraint that their total enthalpy is conserved. Dry–convective adjustment is performed from the lowest to the highest model layer, iteratively.

Middle–level convection occurs if the temperature lapse rate between any two adjacent vertical layers is conditionally unstable and the lower–layer air is sufficiently near saturation that it would be positively buoyant if displaced to the higher layer (Arakawa 1969; Arakawa and Mintz 1974). This condition occurs when the moist static energy of the lower layer exceeds the saturated moist static energy of the upper layer. When the instability exists, an upward convective mass flux occurs between the layers within a convective tower, and a compensating downward mass flux occurs between the layers in the environment outside the convective tower. Because the air within the convective tower is saturated, the convective mass flux therein generates liquid water, part of which is converted into convective precipitation that falls out of the cloud. The subsiding mass flux in the environment modifies the environmental temperature, water vapor and horizontal momentum. This modification of the environment reduces the instability at a rate that depends on the convective mass flux. The latter is calculated such that the instability is removed with an e–folding time of one

hour. The fractional cloudiness for middle–level convective cloud is a function of the convective mass flux and the relative humidity of the higher layer.

Penetrating convection occurs if the temperature lapse rate between the PBL and any layer above is conditionally unstable and the PBL air is sufficiently near saturation that it would be positively buoyant if displaced to the higher layer (Arakawa and Schubert 1974). This condition occurs when the moist static energy of the PBL exceeds the saturated moist static energy of the higher layer. The treatment of penetrating convection is essentially the same as the treatment for middle–level convection, except that: (1) as many convective towers may coexist as there are layers above the PBL, one tower extending from the PBL to each layer for which the instability exists; (2) environmental air is entrained into each convective tower from all layers through which it passes, and this mass transport modifies the temperature and water vapor within the cloud, as well as the temperature, water vapor and horizontal momentum within the environment; and (3) when the initiating instability for any cloud tower ceases to exist, the cloudiness at its top level evaporates with a prescribed e–folding time.

Large–scale condensation occurs in a layer not only when the grid cell is everywhere saturated, but also when only part of the grid cell is saturated (Sundqvist 1978, 1988). The rate of condensation depends on the large–scale convergence rates of moisture, heat and mass, and the time rate of change of fractional relative humidity of the layer, U. The latter is determined from $U = bU_s + (1 - b)U_o$, where b is the fractional cloudiness, $U_s (= 1.006)$ is the supersaturated relative humidity within the cloud, $1 - b$ is the cloud–free fraction, and U_o the fractional relative humidity of the clear air. Closure is achieved by assuming: (1) the moisture convergence is partitioned between the cloud and clear air in proportion to b and $1 - b$, respectively; and (2) $U_o = U_{oo} + b(U_s - U_{oo})$, where U_{oo} is the relative humidity at which condensation can begin. The result is that $b = 1 - [(U_s - U) / (U_s - U_{oo})]^{1/2}$, which increases from zero for $U = U_{oo}$ to unity for $U = U_s$. U_{oo} is taken to be 0.98.

For clouds with temperature below 0°C, a fraction of the cloud water is taken to be ice, with the fraction increasing linearly from zero at 0°C to unity at –30°C. Precipitation occurs in the ice

phase if the cloud temperature is less than 0°C, and in the liquid phase otherwise. The rate of cloud–water conversion to precipitation is ten times larger for the ice phase than for the liquid phase. Large–scale precipitation beneath cloud base evaporates (sublimates) at a rate that is proportional to the product of the precipitation rate, the relative humidity deficit from saturation, and the cloud–free fraction of the grid cell. Convective precipitation beneath cloud base evaporates at a rate that is proportional to the product of the relative humidity deficit and the cloud–water content (Schlesinger *et al.* 1988).

Stratiform and cumuloform clouds can coexist within the same vertical atmospheric column, albeit not in the same layer. A cloud in any vertical layer is identified as either a stratiform or cumuloform cloud depending on the preceding cloud type, the large–scale condensation and the convective mass flux in the layer. If there is convective mass flux, the cloud type is taken to be cumuloform regardless of whether the preceding cloud was stratiform or cumuloform. If there is large–scale condensation and no convection, the cloud is taken to be stratiform. If there is neither convection nor large–scale condensation, the cloud maintains its cloud type until it dissipates by evaporation (Schlesinger and Oh 1993).

(3)   Radiative transfer and radiation–cloud interaction

When we created the first version of the 24–layer ST–GCM from our 11–layer tropospheric GCM (Wang and Schlesinger 1995; Schlesinger *et al.* 1997a; Wang and Schlesinger 1999) we employed the radiative parameterization of the latter (Oh 1989) (hereafter UIUC89). However, that parameterization proved to be unsatisfactory for the stratosphere in the ST–GCM. Inaccurate longwave cooling and solar heating prohibited the model from being integrated forward longer than a month before the model suffered computational instability because of unrealistically strong winds. One major reason for the inaccurate cooling rates is that the Doppler broadening of the absorption lines of water vapor, carbon dioxide and ozone was not taken into account. Accordingly, as described below, we have developed new parameterizations (hereafter UIUC98) for terrestrial (infrared) and solar radiation and their interaction with clouds.

Terrestrial radiation. The UIUC98 parameterization of infrared radiation is based on the parameterization developed by Chou and Suarez (1994) which computes absorption and emission of terrestrial radiation due to water vapor, carbon dioxide and ozone, and contains 8 broad bands ranging in wavenumber from 3000 cm^{-1} to 0 cm^{-1}. The third band (540~800 cm^{-1}) contains three sub–bands to cover the rapid changes of the CO_2 absorption coefficients between the band center and band wings. Depending upon the importance of the scaling effect of the vertical variations of pressure and temperature on absorption, three different approaches are used to compute the transmission functions for different gaseous absorbers: (1) the k–distribution method with linear pressure and/or temperature scaling, (2) two–parameter scaling with precomputed look–up tables, and (3) one–parameter scaling. Chou and Suarez (1994) examined and validated this parameterization against accurate line–by–line calculations. They showed that the scheme is capable of computing the cooling rate accurately for both the middle and lower atmospheres (from 0.01 hPa to the surface) with errors less than 0.4°C/day.

To use the Chou and Suarez (1994) parameterization in the 24–layer ST–GCM, we have modified the parameterization to take into account the influence of clouds, aerosols and trace gases (N_2O, CH_4, CFC–11, CFC–12, and HCFC–22) according to Chou (personal communication 1997). In this UIUC98 version, two–parameter scaling is used for absorption by the centers of the water–vapor bands, the k–distribution method with linear pressure scaling is used for absorption by the wings of the water–vapor bands, and one–parameter temperature scaling is used for the water–vapor continuum absorption. Two–parameter scaling is also used to compute CO_2 and O_3 absorption because Doppler broadening of their absorption lines is important in the upper stratosphere. The transmittances due to trace gases are computed using the k–distribution method with linear pressure scaling. A narrow band in the 15 μm region has been added to account for the flux reduction due to N_2O. The sixth band (1100 ~ 1380 μm) in the Chou and Suarez (1994) parameterization has been divided into two bands (Ming–Dah Chou, personal communication 1997). Table A–1 shows the longwave spectral bands, together with the corresponding absorbers

Table* *A–1. *Longwave spectral bands with corresponding absorbers and methods used to compute transmittances (revised from Table 1 of Chou and Suarez (1994)).*

Band	Wavelength (cm^{-1})	Absorber	Transmittance Calculation Method
1	0–340	H_2O line	two–parameter
2	340–540	H_2O line	two–parameter
3	540–800	H_2O & 15 μm CO_2 overlap H_2O continuum CO_2 N_2O	k–distribution one–parameter two–parameter k–distribution
4	800–980	H_2O line H_2O continuum CO_2 CFC–11, CFC–12, HCFC–22	k–distribution one–parameter k–distribution k–distribution
5	980–1100	H_2O line H_2O continuum O_3 CO_2 and CFC–11	k–distribution one–parameter two–parameter k–distribution
6	1100–1215	H_2O line H_2O continuum N_2O, CH_4 CFC–12, and HCFC–22	k–distribution one–parameter k–distribution k–distribution
7	1215–1380	H_2O line H_2O continuum N_2O and CH_4	k–distribution one–parameter k–distribution
8	1380–1900	H_2O line	two–parameter
9	1900–3000	H_2O line	k–distribution

and methods of computing transmittance. To reduce computing time, the column–integrated absorber amount and absorber–weighted temperature and pressure are assumed not to change within each simulated 6–hour period; thus the transmission functions due to gaseous absorbers are computed only 4 times per day.

To illustrate the importance of this revision of the longwave radiation parameterization in correctly simulating the atmospheric cooling rate, a column radiative–transfer model was constructed using the infrared radiation scheme of our 7–layer tropospheric and 11–layer troposphere/lower–stratosphere GCMs (UIUC89) (Oh 1989), and a second radiative–transfer model was constructed using the new infrared radiation scheme (UIUC98) described above. Both of the 1–D column models extend up to 1 hPa and have identical 24 layers, with sigma values prescribed to be the same as in the 24–layer ST–GCM (Fig. A–2). With the initial profiles of temperature, pressure, ozone and water vapor interpolated from the standard atmosphere of McClatchey *et al.* (1972) to the model layers, and with only the major contributors to longwave cooling (H_2O, CO_2, and O_3) included, the cooling rates (°C/day) are computed for the clear–sky atmospheric conditions of mid–latitude summer, tropics, and sub–arctic winter, separately using the two 1–D radiative–transfer models. Here the CO_2 concentration is taken to be 350 ppmv throughout the atmosphere. Cooling rates (negative) computed from these two models and their differences (UIUC98 minus UIUC89) are presented in Fig. A–3 for the four atmospheric conditions. It is seen from Fig. A–3 that the UIUC89 longwave parameterization is not accurate relative to the UIUC98 parameterization. For the cases of mid–latitude summer and tropics, it overestimated the cooling rates in the stratosphere, with the largest error of about 2°C/day occurring in the middle stratosphere near 10 hPa, and underestimated the cooling rates in the troposphere, except near the surface, with the largest error of about 1.2°C/day occurring near 200 hPa. For the case of sub–arctic winter, the UIUC89 longwave parameterization slightly underestimated the cooling rate in the middle troposphere, but severely overestimated the cooling rate in the upper stratosphere, with a maximum error reaching 4.8°C/day.

Fig. A–3. *Longwave cooling and solar heating rates (°C/day) calculated using two 24–layer column radiative–transfer models, one using the UIUC98 radiation routines of the UIUC 24–layer ST–GCM (labeled as "new") and the other using the UIUC89 radiation routines (Oh 1989) of the UIUC 7–layer and 11–layer AGCMs (labeled as "old"). Four standard clear–sky atmospheric profiles of McClatchey et al. (1972) are considered: mid–latitude summer (upper panels), tropics (middle panels), and the sub–arctic winter for longwave radiation and sub–arctic summer for solar radiation (lower panels). The difference between the longwave cooling rates and the difference between the solar heating rates of the "new" and "old" radiation routines are presented in the right panel for each atmospheric condition. In all panels, only CO_2, H_2O and O_3 are included in the radiative–transfer calculation.*
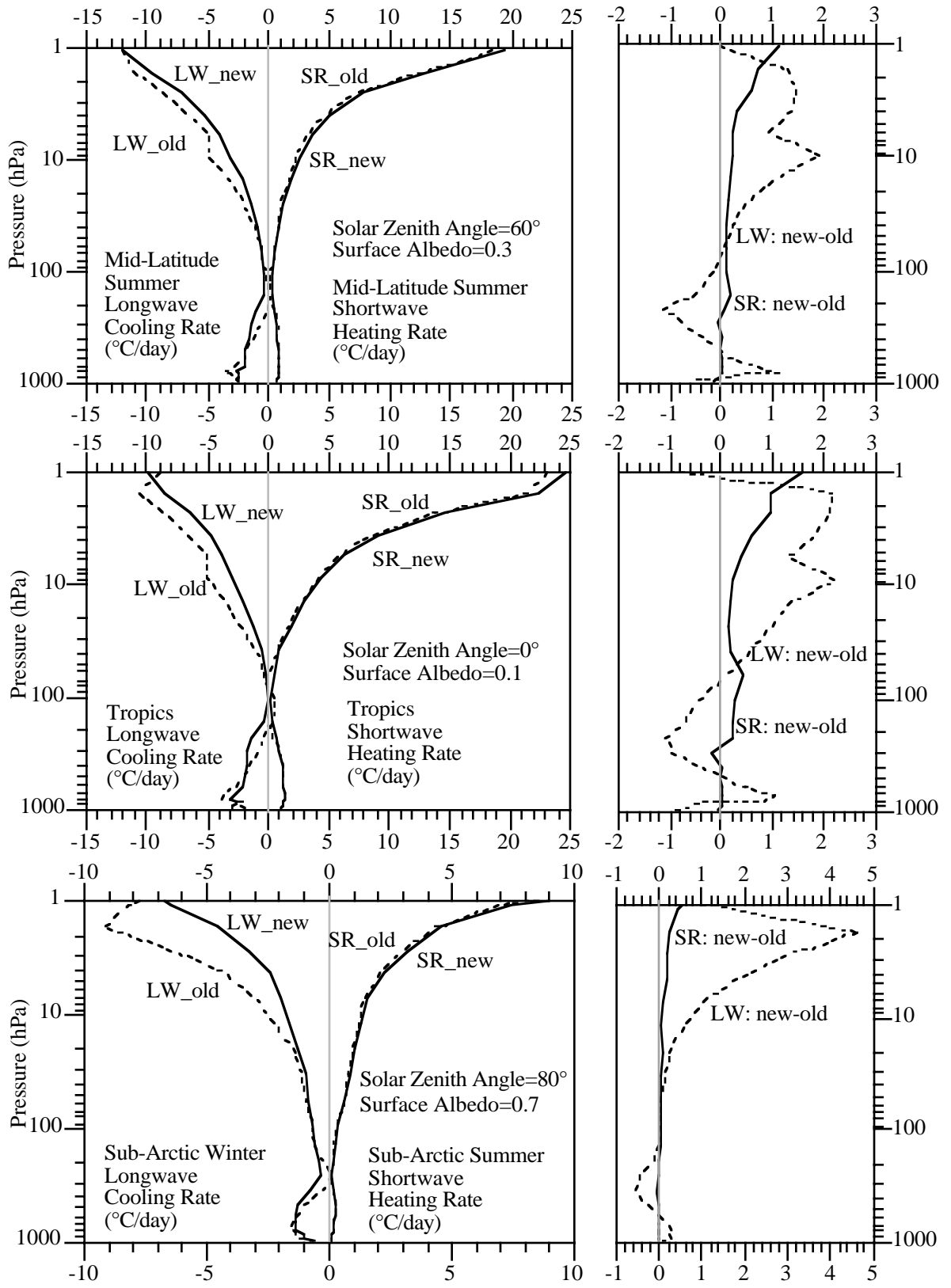
The effects of clouds on terrestrial radiation are included in the UIUC98 parameterization by introducing a mean flux transmittance that is the product of the gaseous transmittances and a cloud–related coefficient (Chou and Suarez 1994). This coefficient is calculated for each GCM layer and conveys information about cloudiness, cloud optical thickness, and cloud overlapping. This approach is flexible enough to allow the choice of the type of cloud overlapping to be used. To be consistent with the solar–radiation parameterization, clouds are grouped into three categories – high clouds above the 16th σ–layer (~ 400 hPa) of the model, middle clouds between the 16th and 19th σ–layers (~ 700 hPa), and low clouds below the 19th σ–layer (see Fig. A–2). Clouds within each category are assumed to be maximally overlapped, while the different cloud categories are assumed to be randomly overlapped. The cloud transmission function for a given layer depends on the cloud liquid and/or ice water path and cloud emissivities, with the latter prescribed following Stephens (1978) for liquid–water clouds and Starr and Cox (1985) and Griffith *et al.* (1980) for ice clouds.

Solar radiation. The UIUC98 parameterization of solar radiation is based on the parameterization developed by Chou (1990; 1992), Chou and Lee (1996), and (Chou and Suarez 1999). We have added the scattering and absorption of aerosols and modified the cloud–radiation interaction. The UIUC98 parameterization computes the absorption by water vapor, ozone, carbon dioxide, oxygen, clouds and aerosols, and the scattering by clouds, aerosols and molecules (Rayleigh scattering). There are 8 bands in the ultraviolet and visible spectral regions (0.175–0.7 μm) and three bands in the near–infrared and thermal–infrared regions (0.7–10.0 μm) (Table A–2). In the first 8 bands, effective coefficients for ozone absorption and effective cross–sections for Rayleigh scattering are pre–computed. In each of the last 3 bands, the k–distribution method with simple pressure scaling is used to calculate the solar heating by water vapor and carbon dioxide. Absorption and scattering of solar radiation by clouds are included in all 11 spectral bands (0.175 μm–10 μm).

Cloud grouping and overlapping are treated in the same way as in the longwave–radiative transfer parameterization. The shortwave radiative properties of liquid–water clouds (Slingo 1989) depend on liquid–water path and the equivalent radius of the drop–size distribution (r_e), the latter

Table A–2. *Optical properties of sulfate aerosol (75% H_2SO_4 and 25% H_2O) computed from a Mie theory model and integrated over the 11 spectral bands of the solar radiation model.*

Solar band	Spectral range (µm)	Specific Extinction (m^2/g)	Single scattering albedo	Asymmetry factor
1	0.175 – 0.225	9.266970	1.000000	0.681185
2	0.225 – 0.245	9.598478	1.000000	0.689153
	0.260 – 0.280	9.752305	1.000000	0.702173
3	0.245 – 0.260	9.700645	1.000000	0.695448
4	0.280 – 0.295	9.755453	1.000000	0.708951
5	0.295 – 0.310	9.715019	1.000000	0.714398
6	0.310 – 0.320	9.653944	1.000000	0.718529
7	0.320 – 0.400	9.205408	1.000000	0.730148
8	0.400 – 0.700	6.556963	1.000000	0.724810
9	0.700 – 1.22	2.608097	0.999987	0.627487
10	1.22 – 2.27	0.555460	0.985749	0.407517
11	2.27 – 10.0	0.383464	0.144101	0.091496

determined by the in–cloud liquid–water content and cloud–droplet number concentration (CDNC). The CDNC is empirically related to the sulfate aerosol mass concentration (Boucher and Lohmann 1995). This approach enables us to study the indirect radiative forcing of sulfate aerosol. Shortwave radiative properties of ice clouds are also functions of the ice–water path and ice crystal effective size, taken to be 70 µm. For mixed–phase clouds, the optical depth is the summation of water–cloud optical depth and ice–cloud optical depth, the single–scattering albedo is optical–depth

weighted, and the asymmetry factor is optical–depth and single–scattering–albedo weighted. The delta–Eddington method is first used to calculate transmittance and reflectance of each layer (King and Harshvardhan 1986), and then the two–stream adding method following equations (3)–(5) of Chou (1992) is applied to compute the upward and downward fluxes in both the clear and cloudy atmosphere.

Two column solar radiative–transfer models with UIUC89 and UIUC98 parameterizations of solar radiation were constructed to compare the solar heating rates. Three clear–sky atmospheric conditions chosen from the McClatchey *et al.* (1972) standard atmospheric profiles were tested with only the major absorbers of solar radiation (H_2O, O_3 and CO_2) included: (1) the mid–latitude summer, with a solar zenith angle of 60° and surface albedo of 0.3; (2) the tropics, with a solar zenith angle of 0° and surface albedo of 0.1; and (3) the sub–arctic summer, with a zenith angle of 80° and surface albedo of 0.7. The calculated heating rates using the UIUC98 and UIUC89 solar radiation schemes and their differences are shown in Fig. A–3, separately, for the three atmospheric conditions. These two schemes result in nearly identical heating rates in the troposphere. In the stratosphere, the heating rate by the UIUC89 scheme is generally smaller than that by the UIUC98 scheme and the discrepancy increases with height. The maximum differences occur near the model top and are 1.1°C/day for the mid–latitude summer, 1.5°C/day for the tropics and 0.4 °C/day for the sub–arctic summer.

(4)   Aerosol

In the ST–GCM the radiative effects of aerosols on terrestrial and/or solar radiation can be turned on in the troposphere and/or stratosphere, depending on the research interest. Both scattering and absorption are included in the solar radiation parameterization, while absorption and emission are included in the terrestrial radiation parameterization. In the present version of the 24–layer ST–GCM, the radiative properties (specific extinction, single–scattering albedo and asymmetry factor) of tropospheric sulfate aerosol have been calculated off–line by our Mie scattering model (Boucher *et al.* 1998). We assume that: (1) aerosol particles consist of 75% sulfuric acid and 25% water, (2) the fraction of fine–particle mass that is sulfate is 60% (Kiehl and Briegleb 1993), and (3)

the aerosol size distribution follows a modified Gamma function (WMO 1986). The complex index of refraction as a function of wavelength follows the WMO report (1986).

The Mie scattering model was run with a high spectral resolution of 0.005 μm to compute the specific extinction, single–scattering albedo and asymmetry factor. These optical properties in high spectral resolution were then integrated to the 11 broad bands of the solar radiation model and the 9 broad bands of the terrestrial radiation model. Table A–2 presents the solar spectral bands, together with the calculated specific extinction, single–scattering albedo and asymmetry factor for sulfate aerosol in each band. The single–scattering albedo for sulfate aerosol is set to be 0 for all bands of terrestrial radiation since scattering is considered negligible there. The spectral extinction efficiency of terrestrial radiation by sulfate aerosol in each band is not shown here. This aerosol model has also been installed in our 11–layer troposphere/lower–stratosphere GCM (Wang 1996; Schlesinger *et al.* 1997a; Wang and Schlesinger 1999), with appropriate modifications, and used to study global and regional climate changes induced by the direct solar radiative forcing of anthropogenic sulfate aerosol (Schlesinger *et al.* 1997b). Simulation results from the 11–layer troposphere/lower–stratosphere GCM have been provided through the Internet (ftp://crga.atmos.uiuc.edu/pub/emf/) for scientists to study the impacts of global and regional sulfate aerosol emissions.

(5) Gravity–wave drag

Gravity waves, excited when stably stratified air flows over irregular terrain, are able to transport horizontal momentum vertically. Parameterization of the drag effect of orographic gravity waves with spatial scales smaller than those resolved by an AGCM's grid is important. Usually unrealistically intense midlatitude eastward surface winds exist in GCMs without parameterization of orographic gravity–wave drag (Hamilton 1996). Other processes, such as moist convection, the development of dynamical instabilities of the Kelvin–Helmholtz type, geostrophic adjustment and frontal zones, can also produce gravity waves and transfer mean momentum between the troposphere and the stratosphere/mesosphere. Non–orographic gravity waves generally have

non–zero phase speeds and are less well understood at present than orographically excited gravity waves.

In the past two decades considerable effort has been made to understand and parameterize gravity–wave drag (GWD), with more attention paid to non–orographic gravity–wave drag in recent years. A few different parameterization schemes of orographically excited gravity–wave drag have been widely used in both numerical weather–prediction models and general–circulation models. Stimulated by Lindzen's (1981) work on the simple parameterization of wave breaking associated with the onset of convective instability, McFarlane (1987) designed a wave–drag parameterization based on linear theory for steady monochromatic waves, with the momentum flux divergence being represented by the wave–saturation assumption, and applied it to the Canadian Climate Center T21 spectral climate model. Palmer *et al.* (1986) independently developed and tested another orographic wave–drag parameterization, also based on Lindzen's wave–saturation hypothesis, in the United Kingdom Meteorological Office gridded general–circulation model.

We have included Palmer *et al.*'s (1986) parameterization of orographically excited gravity–wave drag in the 24–layer ST–GCM. In this parameterization the surface stress is proportional to the near–surface wind speed and static stability, and to the variance of the subgrid–scale orography, and wave breaking depends on the Richardson number. The vertical profile of wind stress is determined by a saturation hypothesis whereby breaking waves are maintained at marginal stability. To use the scheme in the 24–layer ST–GCM, a modification has been made to allow 90% of the horizontal momentum transported by gravity waves to exit the model top if the wave–breaking level does not occur within the model. This scheme requires tuning of several parameters to obtain the best wave–breaking effect, for example, the subgrid–scale mountain wavenumber and the upper limit of the subgrid–scale mountain–height variance.

To determine the effect of the parameterized GWD on the 24–layer ST–GCM's performance, two 180–day perpetual–January simulations have been performed, one with the GWD parameterization and one without. The first 60 days of each simulation are taken as spin–up time, and the last 120 days of each simulation are used for comparison. Fig. A–4 shows the sea–level
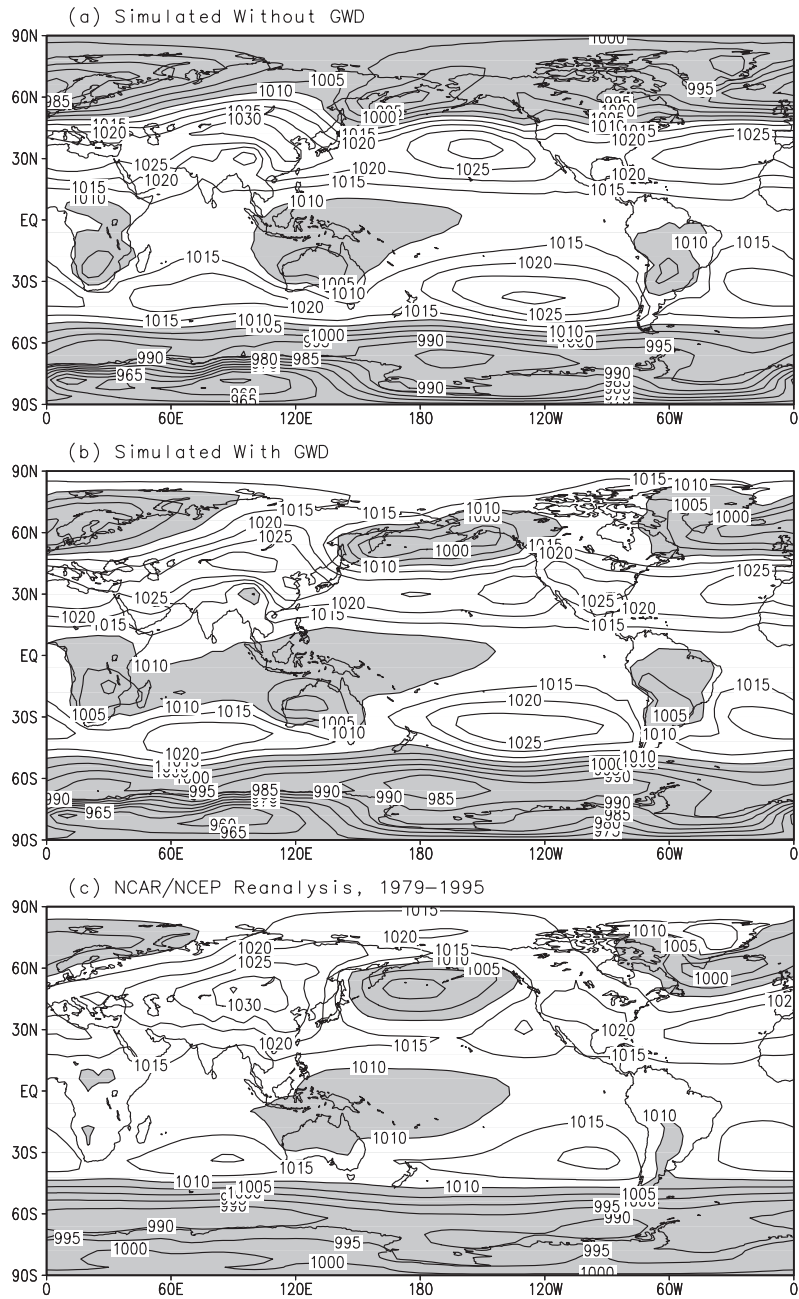
Fig. A–4. *Comparison of sea–level pressure fields between two perpetual–January simulations without (a) and with (b) GWD parameterization. In each 180–day simulation the data from the last 120 days were saved to derive the mean sea–level pressure. The observed in (c) is from the NCEP/NCAR Reanalysis averaged from 1979 through 1995. Pressure values less than 1010 hPa are shaded.*

pressure averaged over the last 120 days of the two simulations, together with the observed January sea–level pressure climatology derived from the NCEP/NCAR Reanalysis averaged from 1979 through 1995, which is provided on the Internet by the Climate Diagnostics Center, U.S. Department of Commerce, NOAA (http://www.cdc.noaa.gov/cdc/data.nmc.reanalysis.html). Distinguishable differences exist in the Northern Hemisphere between the simulated sea–level pressure fields with and without GWD. With GWD, the Icelandic and Aleutian Lows, and the Siberian and North American Highs, are well simulated compared to the observations, though the subtropical High in the Pacific is still about 10 hPa stronger than observed. The overly intense surface westerly winds in the northern–hemisphere middle latitudes in the simulation without GWD are greatly reduced by the GWD parameterization.

Fig. A–5 shows the zonal–mean zonal wind and zonal mean–temperature averaged over the last 120 days of the two simulations, together with observation for January. The observed wind and temperature below 10 hPa are derived from the NCEP/NCAR Reanalysis averaged from 1979 through 1995, and above 10 hPa from the COSPAR International Reference Atmosphere 1986 (CIRA–86) (Rees *et al.* 1990), which is maintained by the British National Space Science Data Center. The CIRA–86 data cover latitudes only from 80°S to 80°N. With GWD the simulated tropospheric westerly centers have about their observed positions and magnitudes, especially in the Northern Hemisphere. The influence of the GWD parameterization on the southern–hemisphere circulation is negligible. Unfortunately, the simulated polar–night jet in the northern lower stratosphere at about 10 hPa is too weak and is shifted equatorward of its observed position. The simulated zonal–mean temperature in the northern polar stratosphere between 100 hPa and 10 hPa is about 10°C warmer than observed with the GWD parameterization, and about 15°C colder than observed without the GWD parameterization.

Palmer *et al.* (1986) performed two perpetual–January simulations using the UKMO 11–layer GCM with and without the GWD parameterization included. They found a temperature difference of about +20°C near the tropopause in the Northern Hemisphere and a zonal–mean zonal wind decrease of about 20 m/s near the top of the model centered in the mid–latitudes. All information indicates
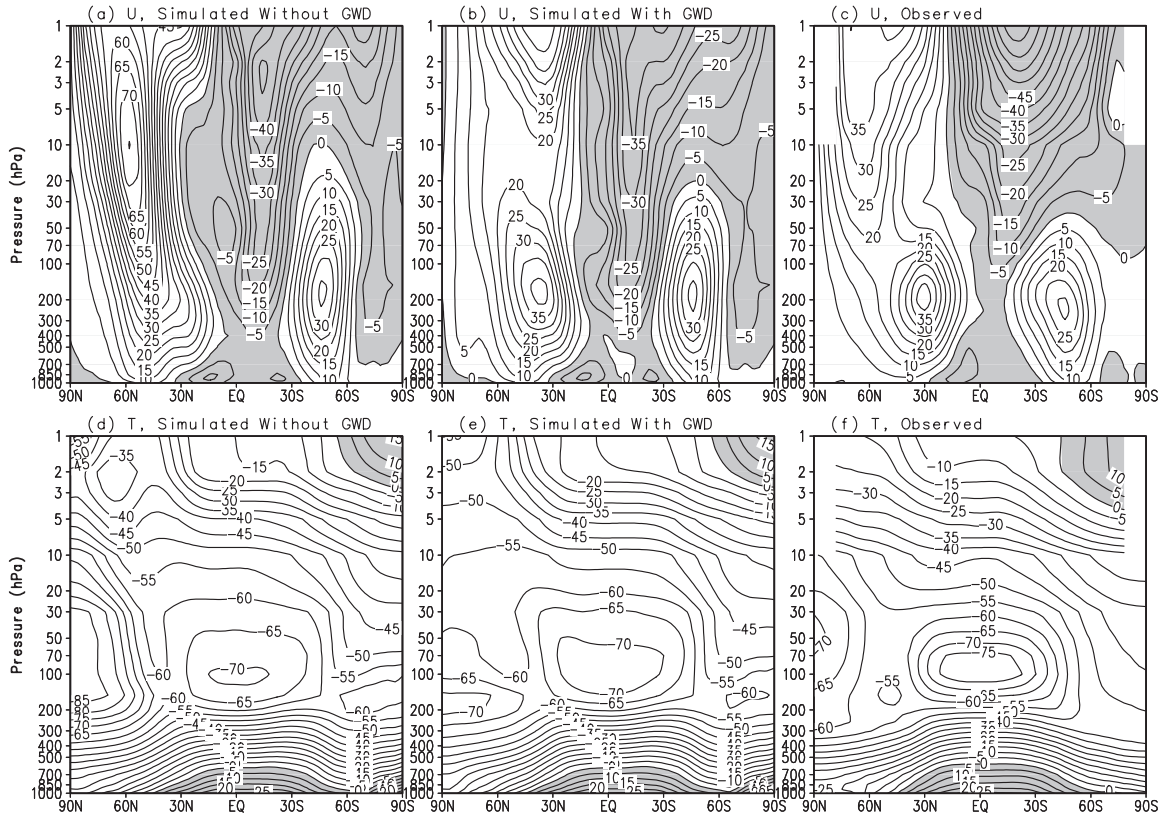
Fig. A–5. *As in Fig. A–4, except for zonal–mean zonal wind (upper panels) and temperature (lower panels). Easterly wind and temperature above 0°C are shaded. The observed wind and temperature below 10 hPa are from the NCEP/NCAR Reanalysis averaged from 1979 through 1995, and above 10 hPa from the COSPAR International Reference Atmosphere 1986 (CIRA–86) (Rees et al. 1990).*

that our GCM might have suffered excessive wind deceleration in the northern lower stratosphere, which in turn causes excessive warming in the northern polar stratosphere. Based on this conjecture, we have conducted a set of perpetual–January simulations by changing the tunable parameters within the GWD scheme and/or by applying the GWD parameterization for the troposphere or the troposphere and lower stratosphere alone. We changed the upper limit for the variance of the subgrid–scale orography (denoted as H) from 200 m to 1000 m, and the representative horizontal wavenumber of the subgrid–scale orography from 1.0×10^{-4} to 0.6×10^{-5} (denoted as K). Unfortunately, none of these simulations proved to be satisfactory. In one extreme, if H and/or K are too small (H = 200 m, K = 0.6×10^{-5}), the GWD parameterization has no detectable effect. The simulated northern polar–night jet is too strong and not separated from the tropospheric subtropical jet, and the simulation of sea–level pressure is not improved. In the other extreme, if H and/or K are too large (H = 1000 m, K = 1.0×10^{-4}), the northern polar–night jet and the tropospheric subtropical jet are separated, but the northern polar–night jet becomes too weak and its core in the lower stratosphere is shifted to the mid–latitudes, and a large warm bias occurs in the northern polar region. The best choice we found for the 24–layer ST–GCM is to set H = 700 m and K = 2.5×10^{-5}, and apply the GWD parameterization to the entire atmosphere, as used in the above perpetual–January simulation.

Despite this shortcoming of the GWD parameterization, we have decided to keep it presently in the UIUC 24–layer ST–GCM for three reasons. First, it does greatly improve the simulation in the troposphere and near the surface. Second, how to parameterize tropospheric/lower stratospheric subgrid–scale GWD in GCMs is still not settled. It is even less clear than how to parameterize subgrid–scale GWD in the mesosphere. Some basic questions remain to be solved (SPARC 1998). Third, some improved GWD parameterization schemes that can resolve the spectral property and different sources of subgrid–scale gravity waves have been developed recently (e.g., Alexander and Dunkerton 1998; Hines 1997a,b) and are being tested. For example, the scheme developed by Alexander and Dunkerton (1998) can be applied in principle to subgrid–scale gravity waves in

GCMs generated by mountains, tropical convection, and wind shear. We look forward to evaluating these newly developed GWD parameterizations in the future.

3. Simulation of the Present Climate

Here, we present results from a 15–year control simulation of the model. For this simulation the distributions of sea–surface temperature and sea ice were prescribed from the AMIP–II monthly mean distributions, which are the averages from 1979 through 1996 (Gleckler 1999), and were updated daily by interpolation between consecutive monthly mean values. The recommended 3–dimensional ozone data (Wang *et al.* 1995) by the AMIP–II panel were used. Tropospheric natural sulfate aerosol from Langner and Rohde's (1991) slow–oxidation simulation was included in the model as tropospheric background aerosol, and only its direct radiative effect – scattering and absorption of solar radiation and absorption of longwave radiation – was included. The effective radius of water cloud droplets was taken to be 12 μm rather than relating it to the aerosol concentration as described in Section 2. Therefore, neither the direct nor the indirect radiative forcing of anthropogenic sulfate aerosol were included in this simulation since their uncertainties are still large, especially the indirect part (Houghton *et al.* 1996).

If not indicated specifically, model results presented below are averages over the last 12 years of simulation. Simulated quantities are compared with observations. Section 3a presents surface–air temperature, precipitation, cloud cover, and cloud–radiative forcing. Section 3b examines atmospheric temperature and circulation, polar vortex, sudden stratospheric warming, the quasi–biennial oscillation (QBO), and the equatorial semi–annual oscillation. Section 3c illustrates the Transformed–Eulerian–Mean circulation and eddy forcing of zonal–mean zonal wind.

a. Surface Quantities, Clouds and Radiative Fluxes

(1) Surface–air temperature

In the model, surface–air temperature is obtained by extrapolating the air temperature at the lowest model level, which is about 80 m above the ground in global average, downward to the surface with a lapse rate of 6.5°C/km. Presented in the left–hand panels of Fig. A–6 are the

simulated annual mean surface–air temperature, the standard deviation of monthly mean surface–air temperature, which measures the variation of surface–air temperature in a year, and the march of zonal–mean monthly mean temperature from January to December. For a better view of the seasonal cycle, the temporal march is repeated for two years. Corresponding observations derived from the NCEP/NCAR Reanalysis averaged from 1979 through 1995 are presented in the right–hand panels of Fig. A–6. The model simulates well the annual–mean surface–air temperature over land, except over Antarctica and Greenland, where the simulated temperature is about 3°C to 6°C warmer than observed. This bias is mainly caused by the smoothed model topography used. Over the ocean, the bias is generally less than 1°C except over the Arctic. The figures of standard deviation and temporal march show that the model describes well the magnitude and phase of the variation of monthly mean surface–air temperature over the globe, except over Antarctica where the simulated standard deviation is much smaller than observed.

(2)　Precipitation

Daily precipitation rates (mm/day) are presented in Fig. A–7 in the same format as in Fig. A–6. The observations are averages from 1979 through 1996 (Xie and Arkin 1997). The model does capture the relative dry condition over northern Africa, western Australia, southern Africa, the two polar regions and the west coast of the American continents, and the relative wet condition over the tropics and the southeastern Asia. The observed large precipitation rates over the warm pool and the Gulf associated with penetrative convection are simulated. The seasonal variation of tropical heavy precipitation associated with the north–south shift of the ITCZ is also captured. However, the model slightly overestimated precipitation over the western tropical Pacific and underestimated over the eastern tropical Pacific. The model also overestimates precipitation over the Eurasian and North American continents in DJF and MAM (not shown).

(3)　Cloud cover

The simulated and observed monthly mean cloud cover (%) is presented in Fig. A–8 in the same format as in Fig. A–6. The observed cloud cover is derived from the ISCCP climatology (Rossow *et al.* 1991). The model simulates well the annual–mean cloud cover and the march of
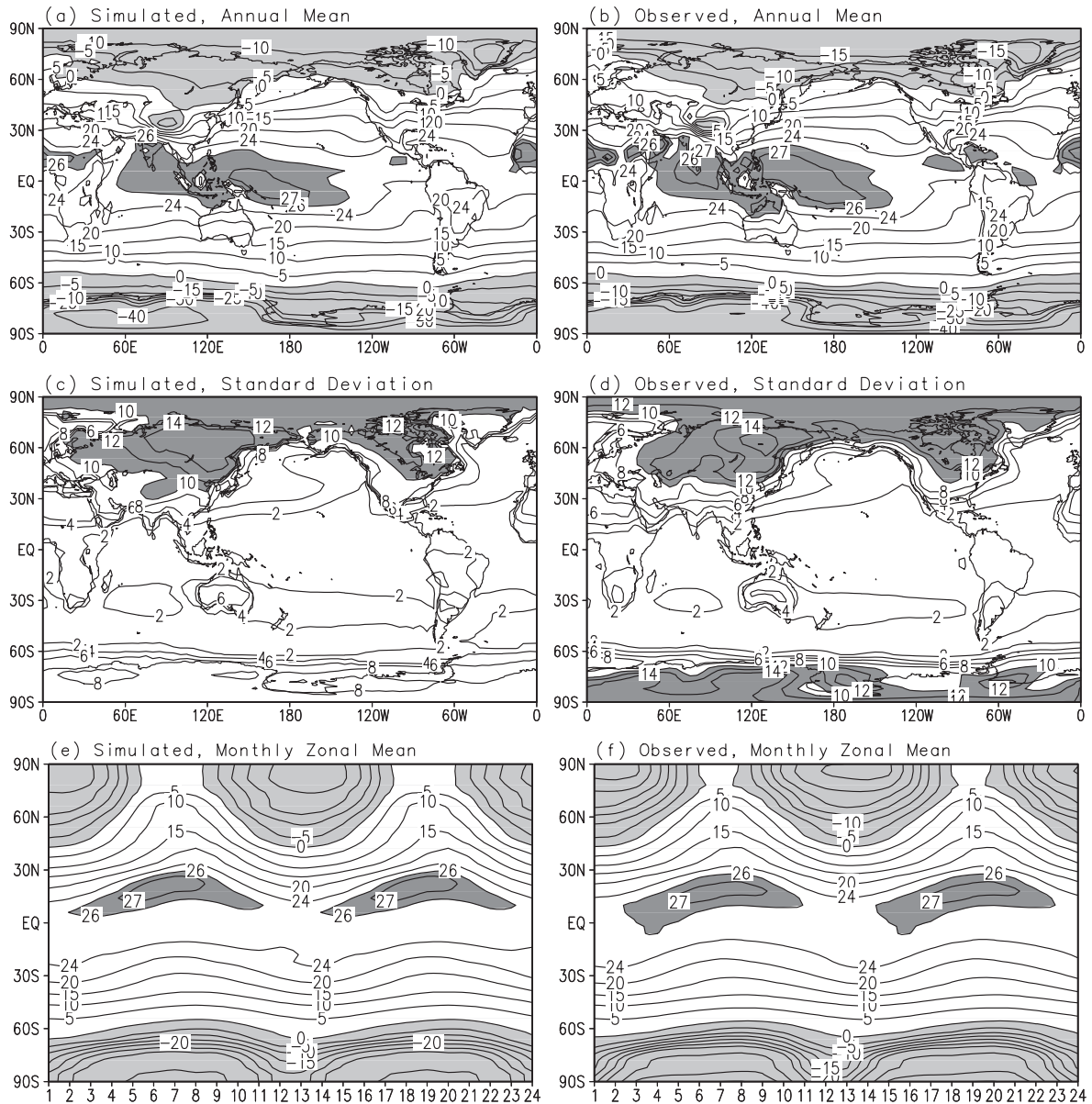
Fig. A–6. *Simulated (left–hand panels) and observed (right–hand panels) annual–mean surface–air temperature in (a) and (b), standard deviations of monthly mean surface–air temperature in (c) and (d), and temporal marches of monthly mean zonal–mean temperature in (e) and (f). For a better view of the seasonal cycle, temporal marches are repeated for two years. In (a), (b), (e) and (f), temperatures higher than 26°C are heavily shaded and below 0°C are lightly shaded. In (c) and (d), standard deviations larger than 10°C are shaded. The observed temperatures are from the NCEP/NCAR Reanalysis averaged from 1979 through 1995.*
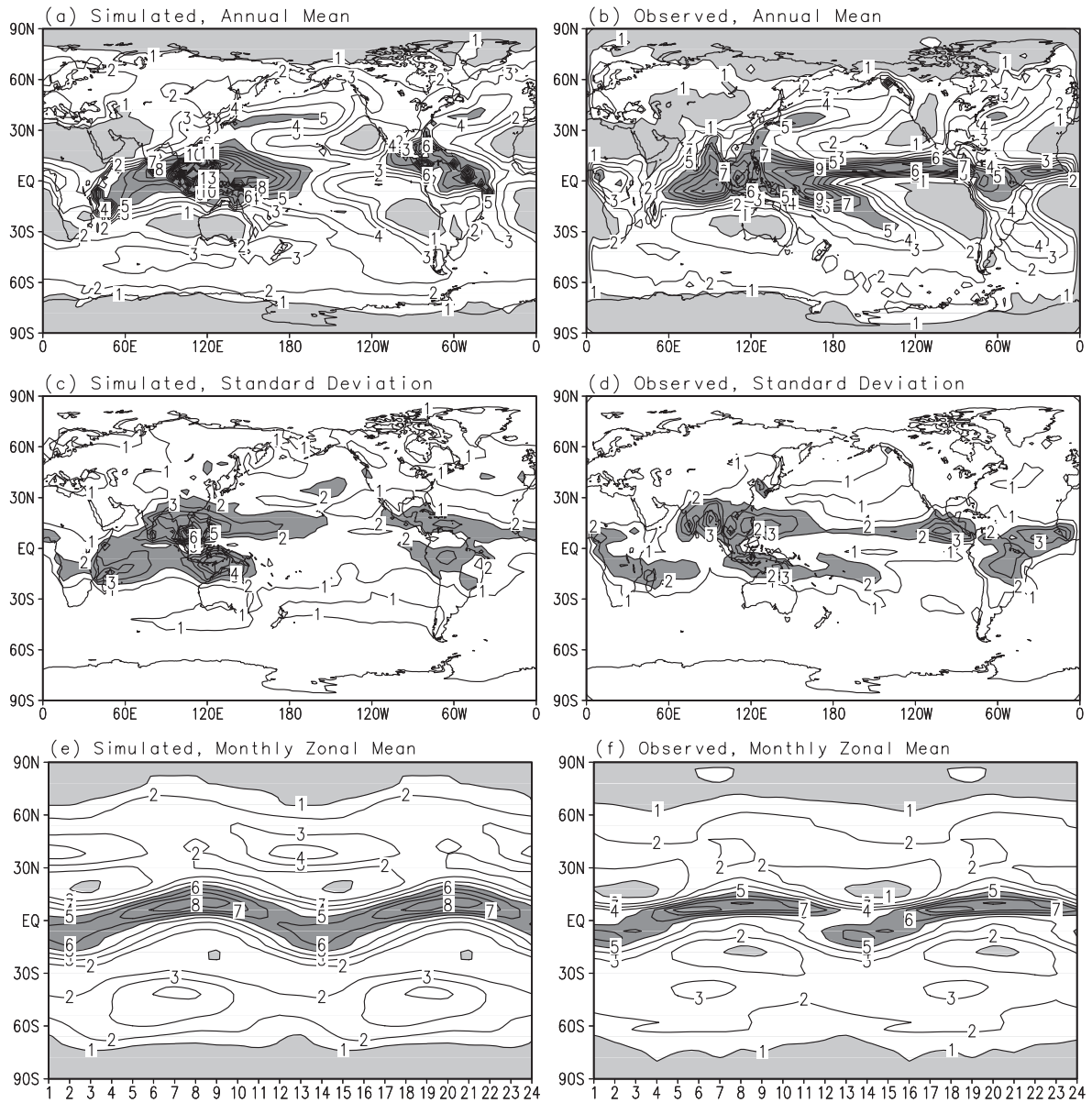
Fig. A–7. *As in Fig. A–6, except for precipitation rate (mm/day). In (a), (b), (e) and (f), precipitation rates larger than 5 mm/day are heavily shaded and smaller than 1 mm/day are lightly shaded. In (c) and (d), standard deviations larger than 2 mm/day are shaded. The observed are averages from 1979 through 1996 (Xie and Arkin 1997).*
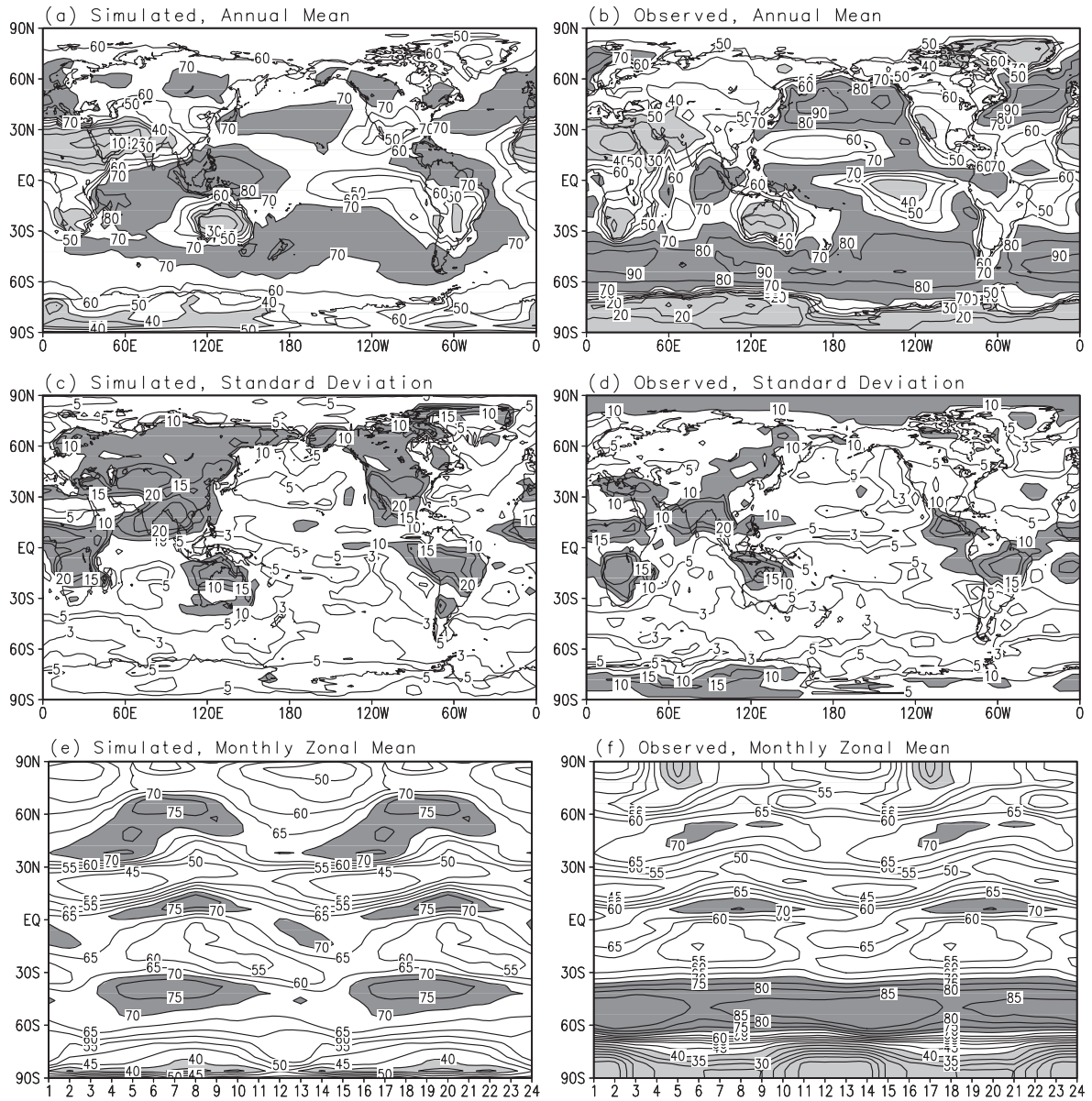
Fig. A–8. *As in Fig. A–6, except for cloud cover (%). In (a), (b), (e) and (f), cloud cover larger than 70% is heavily shaded and smaller than 40% is lightly shaded. In (c) and (d), standard deviations larger than 10% are shaded. The observed are ISCCP climatology (Rossow et al. 1991).*

zonal–mean cloud cover in time in the Northern Hemisphere and north of 50°S in the Southern Hemisphere. Similar to the observations, there are generally more clouds simulated over the oceans than over the continents, and over warm oceanic regions than over cold oceanic regions. The simulated minimal cloud cover over the Sahara, western Australia and the eastern Pacific along the Chilean and Peruvian coasts, and the maximal cloud cover over the warm pool and the Amazon are in good agreement with the observations. The model slightly underestimated the cloud cover over the North Pacific and North Atlantic, and overestimated the cloud cover over northern Eurasia. Zonally averaged, the simulated cloud cover is about 5% larger than observed in the northern middle latitudes in all seasons except DJF. Large errors exist in the high latitudes of the Southern Hemisphere. The model underestimated cloud cover by 20% to 30% along the coast of Antarctica.

We found that the scheme used in the model to diagnose the large–scale fractional cloud, which is based on Sundqvist (1978, 1988), is very sensitive to relative humidity. In high latitudes and near the poles, clouds are formed mainly through large–scale condensation. As described in Section 2, large–scale fractional cloud is $b = 1 - [(U_s - U)/(U_s - U_{oo})]^{1/2}$, where U_s is the saturated relative humidity within the cloud, U the actual relative humidity in the grid cell, and U_{oo} the relative humidity at which condensation can begin. If $U < U_{oo}$, $b = 0$. When we first tuned the model, we set U_s to be 100%, and had to set U_{oo} as large as 99% to obtain a simulated global–mean cloudiness of about 60%. In this case, it is difficult to form large–scale clouds in high latitudes and near the poles because U is usually less than $U_{oo} = 99\%$ there. Consequently, clouds are mostly convective clouds, although some stratiform clouds do form in the tropics and the subtropical lower troposphere. If we increase U_s, b will be smaller for any given U and U_{oo}. Then, the global–mean cloudiness becomes smaller. To compensate for this we can decrease U_{oo} to increase b in order to keep the global–mean cloudiness unchanged. This decreased U_{oo} allows some large–scale clouds to form in high latitudes and near the poles since the condition $U > U_{oo}$ is more easily satisfied for a smaller U_{oo}. It turns out that b is very sensitive to U_s. Fig. A–9 shows the variations of b versus U for three cases: Case A, $U_s = 100\%$ and $U_{oo} = 99\%$; Case B,

U_s=100.5% and U_{oo}=99%; and Case C, U_s=100.5% and U_{oo}=98%. The difference of b between Case A and Case B increases quickly as U increases, and reaches 58% at U=100%. In the current version of the 24–layer ST–GCM, U_s=100.6% and U_{oo}= 98% were used. This change did improve the simulation of cloud amount in high latitudes and near the poles compared to what we obtained with U_s=100% and U_{oo}=99%.
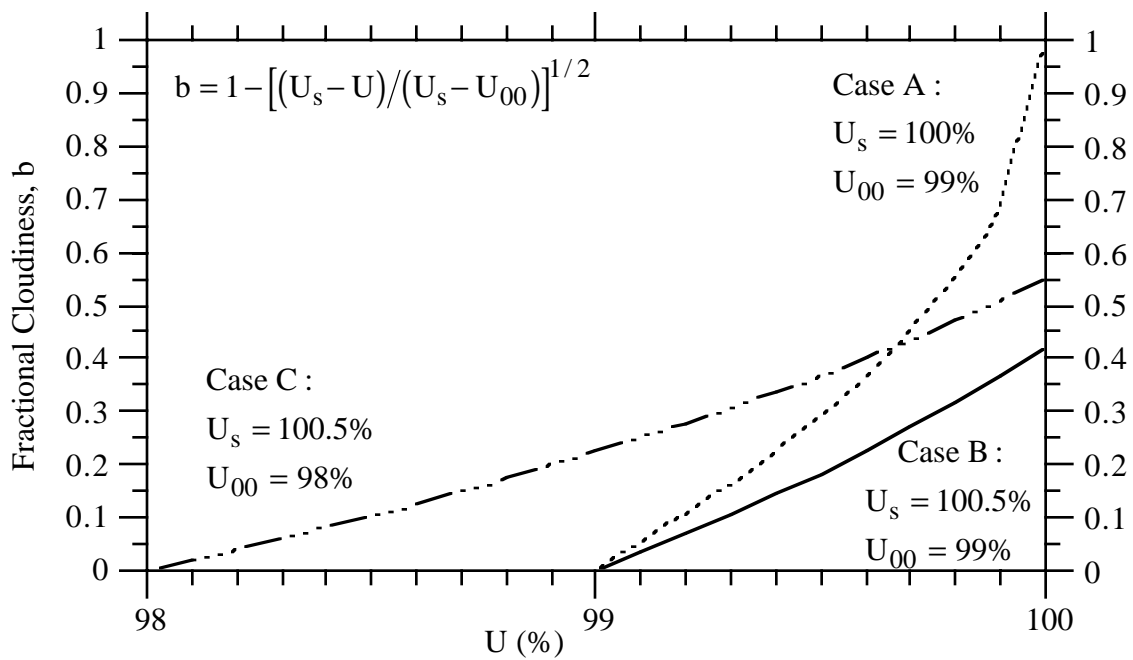

$$b = 1 - \left[(U_s - U)/(U_s - U_{00}) \right]^{1/2}$$

Case A :
$U_s = 100\%$
$U_{00} = 99\%$

Case C :
$U_s = 100.5\%$
$U_{00} = 98\%$

Case B :
$U_s = 100.5\%$
$U_{00} = 99\%$

Fractional Cloudiness, b

U (%)

Fig. A–9. *Variations of fractional cloudiness versus relative humidity for large–scale condensation.*

(4) Cloud radiative forcing

We define the net radiative flux as $N = S - R$, where S is the net incoming solar flux, defined as positive downward, and R is the outgoing terrestrial flux, defined as positive upward. Cloud radiative forcing is given by $CRF = \Delta N = \Delta S - \Delta R$ at the top of the atmosphere (TOA), where Δ is the difference between the all–sky (cloudy sky) and clear–sky radiative fluxes. Positive

(negative) CRF indicates that clouds radiatively heat (cool) the earth–atmosphere system (Cess *et al.* 1997). CRF contains two components, the LW CRF = –ΔR, which is the difference of TOA outgoing longwave radiation (OLR) between cloudy sky and clear sky, and SW CRF = ΔS, which is the difference of TOA net incoming solar radiation between cloudy sky and clear sky. LW CRF is generally positive since clouds trap the outgoing longwave radiation in the atmosphere like greenhouse gases. SW CRF is generally negative since clouds reflect more incoming solar radiation back to space than they absorb. The LW CRF and SW CRF are presented in Figs. A–10 and A–11, respectively, in the same format as in Fig. A–6. We derived the observed climatological CRF components from the ERBE measurements from 1985 through 1989, which were provided by the NASA Langley Research Center, EOSDIS Distributed Active Archive Center.

The height of the cloud tops greatly influences the magnitude of the LW CRF (Cess *et al.* 1997). Generally, the model simulates well the geographical distribution and seasonal variation of the LW CRF, except between 40°S and 60°S, where the model does not simulate cloud cover well (Fig. A–8). The maximum LW CRF in the tropics and its north–south shift from month to month along with the ITCZ are in good agreement with the observations.

When tuning the model, special attention was given to the simulation of the OLR over the warm–pool region, where a regional minimum OLR occurs over the high–SST surface because of the low emission temperature at the top of convective clouds. Wang and Schlesinger (1995, 1999) found that in order to correctly simulate the tropical intra–seasonal oscillation using the UIUC 11–layer AGCM with any of the three convection schemes — the UIUC GCM's cumulus–convection scheme that includes a modified Arakawa–Schubert (1974) penetrative convection scheme and a mid–level convection scheme (Oh 1989), Kuo's (1974) scheme, and Manabe *et al.*'s (1965) moist convective adjustment scheme – a large relative–humidity criterion, usually greater than 80%, must be applied as a threshold for the onset of convection. However, when this constraint was applied to the 24–layer ST–GCM, the simulated penetrating convection in the tropics was too weak and the cloud tops were too low. This led to a 20 to 30 W/m^2 higher–than–observed OLR in the warm–pool region and the resulting LW CRF was too small. It is
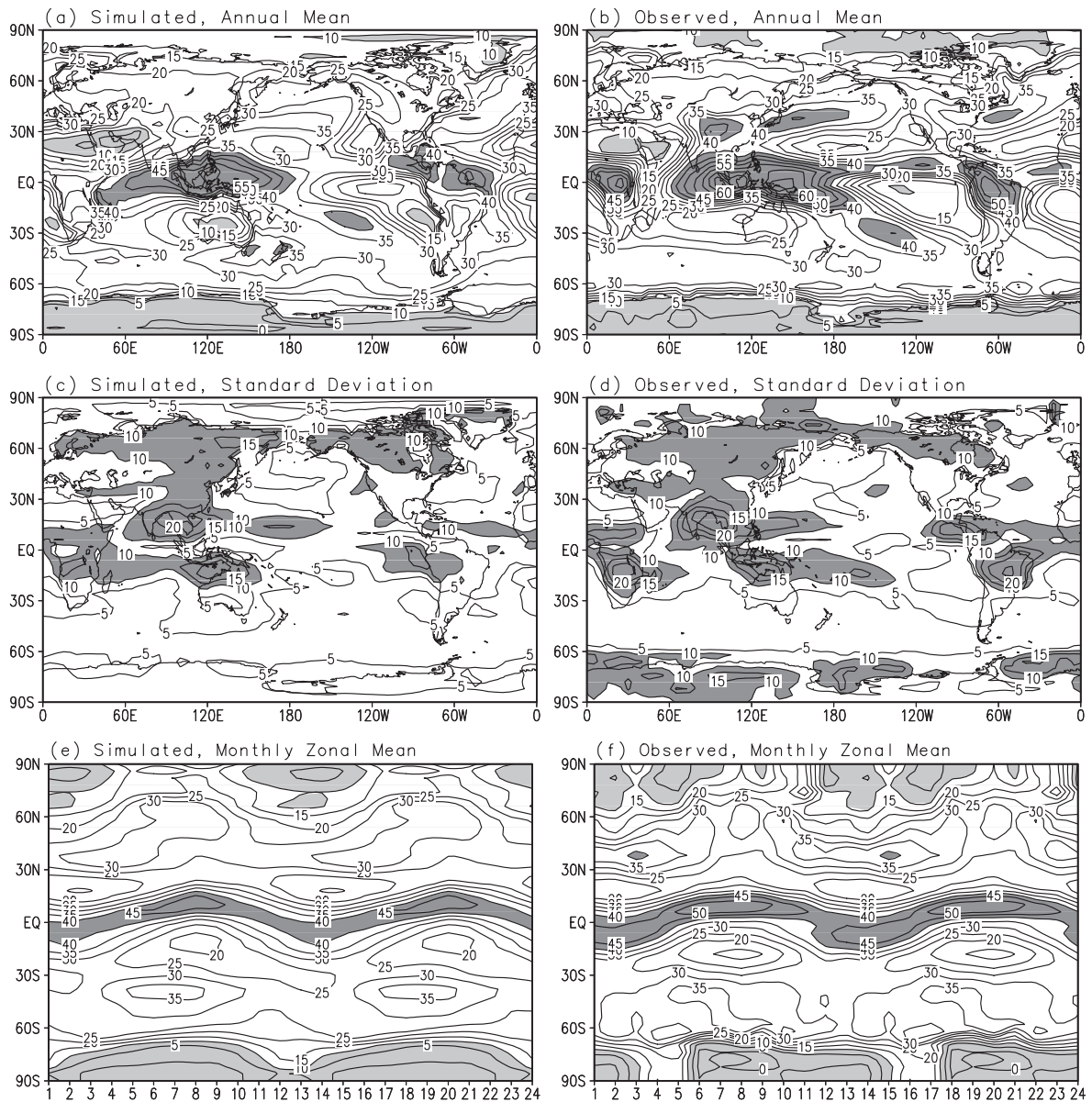
Fig. A–10. *As in Fig. A–6, except for all–sky longwave cloud radiative forcing (LW CRF, W/m²). In (a), (b), (e) and (f) forcing values larger than 40 W/m² are heavily shaded and smaller than 10 W/m² are lightly shaded. In (c) and (d) standard deviations larger than 10 W/m² are shaded. The observations are the averages of the ERBE satellite data between 1985 and 1989.*
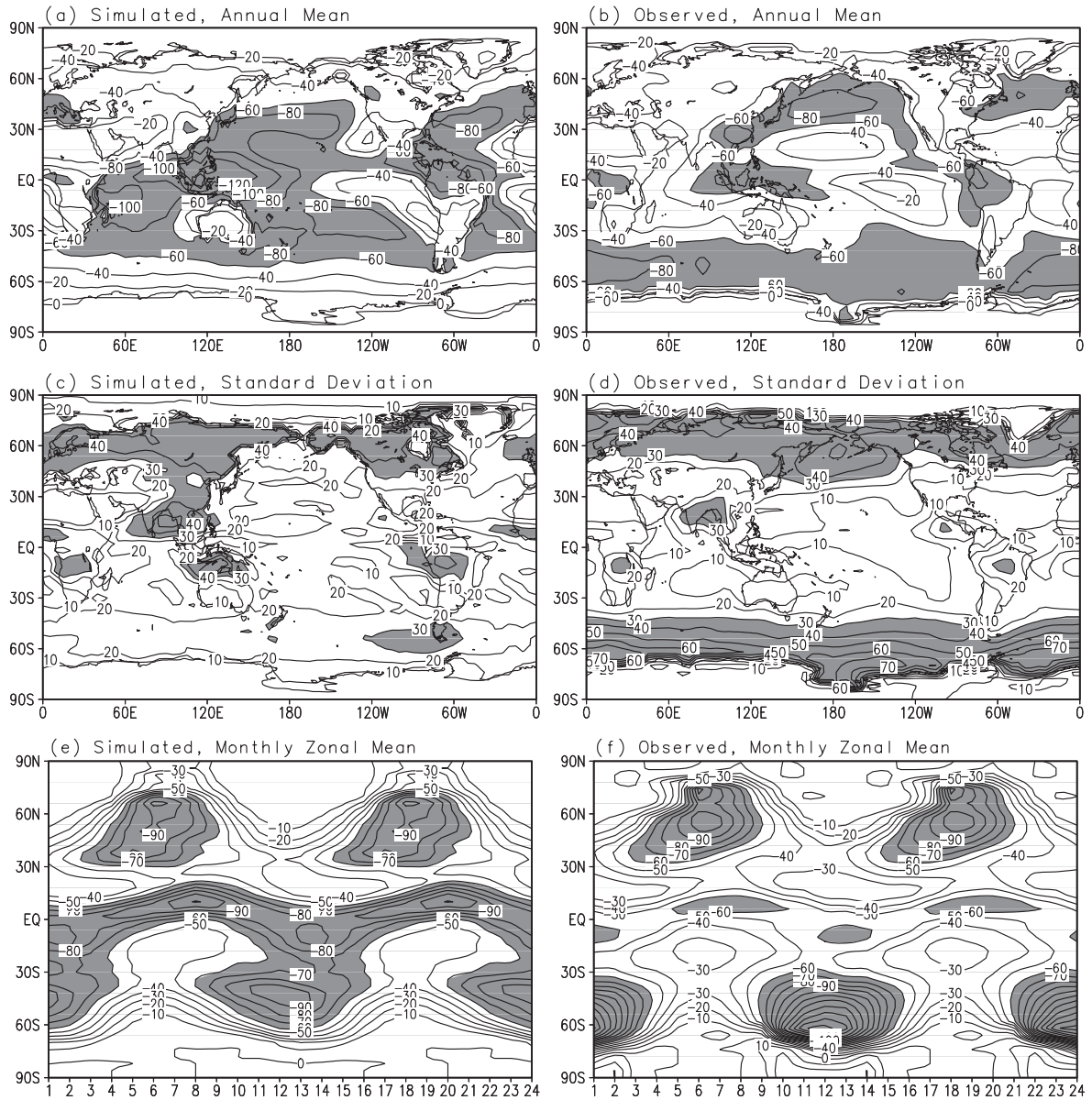
Fig. A–11. *As in Fig. A–10, except for all–sky shortwave cloud radiative forcing (SW CRF, W/m². In (a), (b), (e) and (f) forcing values smaller than –60 W/m² are shaded. In (c) and (d) standard deviations larger than 30 W/m² are shaded.*

found that for the 24–layer ST–GCM a relative–humidity criterion of 50% best reproduces the observed LW CRF over the tropics. This criterion also yields a better simulation of the observed geographical distributions of precipitation and clouds, especially the distinct land–ocean contrast of cloud cover in the northern–hemisphere mid–latitudes. The effect of this revised criterion on the 24–layer ST–GCM's ability to simulate the tropical intra–seasonal oscillation remains to be analyzed.

The model captures the basic geographical distribution and seasonal variation of the SW CRF (Fig. A–11). The model simulates the SW CRF better in the Northern Hemisphere than in the Southern Hemisphere and much better over the continents than over the oceans. Large errors exist over cloud–covered areas in JJA. Generally, the model overestimated the SW CRF in the tropics and subtropics, but underestimated the SW CRF in high latitudes. The largest bias occurs near 60°S in January. This occurs because the model underestimates cloud cover by as much as 20~30% there. In addition to the simulated total cloud cover and the vertical distribution of cloudiness, the prescribed surface albedo also greatly influences the distribution of SW CRF. Fig. A–12 shows the geographical distributions of the simulated clear–sky planetary albedo and their percentage differences from the ERBE observations in January and July. It can be seen that in both months the simulated clear–sky albedo is smaller than observed over open–water surface. The simulated global annual–mean clear–sky albedo is 11.2% smaller than observed. The source of the discrepancy may come from the schemes used to calculate the surface albedo over open water for direct and diffusive solar fluxes. In the model, the surface albedo is fixed to be 0.07 for diffusive solar flux, and is a function of solar zenith angle for direct solar flux (Briegleb *et al.* 1986).

In this section we have compared the geographical distributions and seasonal variations of the simulated surface–air temperature, precipitation, cloud cover and cloud radiative forcing with observations. In Table A–3 we present their annual means over the globe and over the warm pool (10°S–10°N; 140°E–170°E). We also include in Table A–3 the outgoing longwave radiation and net incoming solar radiation at the top of the atmosphere in all–sky and clear–sky conditions, which are used to derive the cloud radiative forcing. Generally, the simulated magnitudes of these quantities
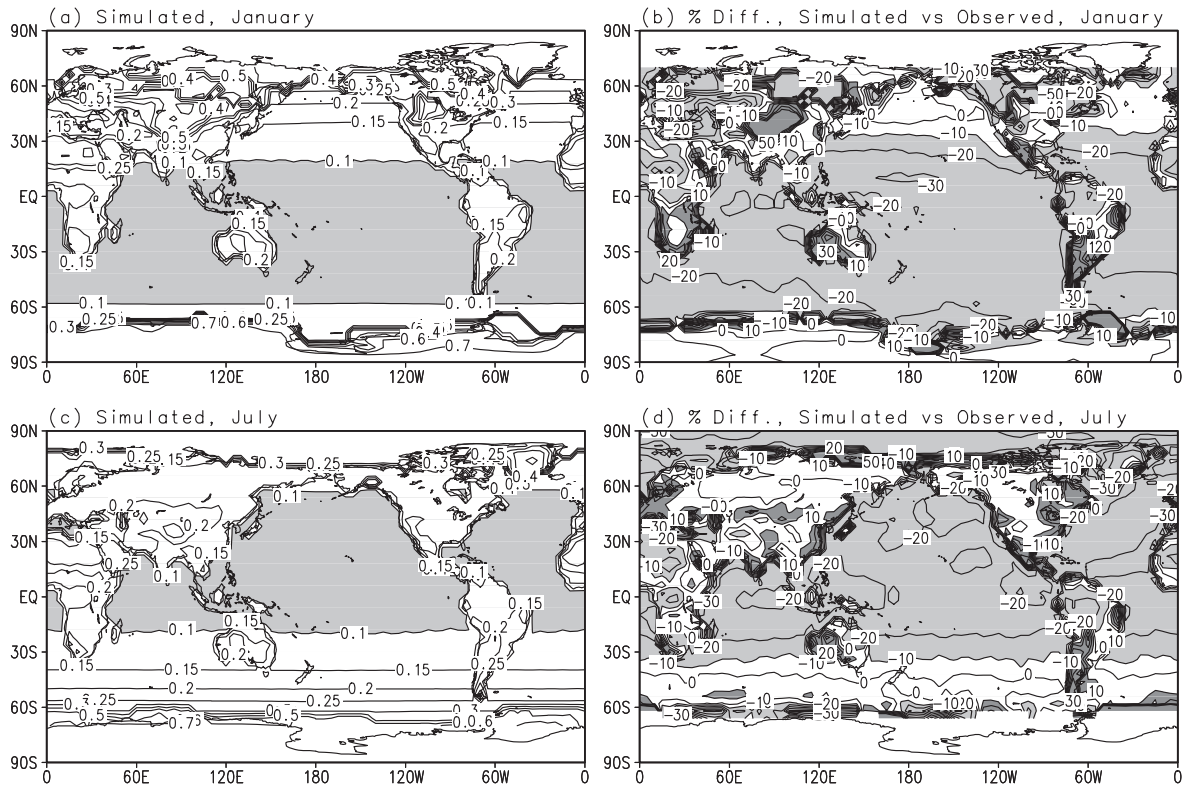
Fig. A–12. *Simulated clear–sky planetary albedo in (a) January and (c) July, and their percentage differences from the ERBE satellite observations in (b) January and (d) July. In (a) and (c) planetary albedos smaller than 0.1 are shaded. In (b) and (d) percentage differences larger than 10% are heavily shaded and smaller than –10% are lightly shaded.*

Table A–3. *Global and warm–pool averages of selected annual–mean quantities from model simulation and observations.*

Quantity		Global Mean		Warm Pool (10°S~10°N; 140°E~170°E)	
		Simulation	Observation	Simulation	Observation
Surface–Air Temperature (°C)		13.9	14.2	26.7	27.4
Cloud Cover (%)		62.4	62.2	78.0	71.6
Precipitation (mm/day)	Large–Scale	1.28	–	1.85	–
	Convective	1.68	–	6.69	–
	Total	2.96	2.67	8.54	8.33
TOA OLR (W/m²)	All–Sky	–237.6	–235.3	–236.0	–227.9
	Clear Sky	–264.8	–264.6	–284.0	–285.7
	LW CRF	27.2	29.3	48.0	57.8
TOA Net SW (W/m²)	All–Sky	239.2	240.2	273.9	309.3
	Clear–Sky	294.3	287.9	380.4	371.9
	SW CRF	–55.1	–47.7	–106.5	–62.6

Source of Observation:

Surface–Air Temperature, NCEP/NCAR Reanalysis, averages from 1979 through 1995;

Cloud Cover, ISCCP Climatology (*Rossow et al.* 1991);

Precipitation, *Xie and Arkin* (1997);

TOA OLR and TOA Net SW, ERBE satellite observation, averages from 1985 through 1989.

match the observed well over the globe and the warm–pool area. One exception is the all–sky TOA net incoming solar radiation over the warm pool. The simulated is 35 W/m^2 smaller than the observed by ERBE. This large discrepancy can be explained in part by the overestimated cloud cover over the warm pool –Table A–3 shows that the simulated cloud cover is 78% and the observed is 71.6%. Another possible explanation is that the model may have underestimated the absorption of solar radiation by clouds over the warm pool. Such an underestimation has been found in many other GCMs and been discussed widely (e.g. Cess *et al.* 1995; Ramanathan *et al.* 1995). Over the warm pool, the simulated clear–sky TOA OLR matches the observed well, but the all–sky TOA OLR is 8 W/m^2 larger than observed. This indicates that the cloud top of convective cloud in the warm–pool area may still not be high enough, even though a relative–humidity criterion of 50% has been used for the onset of convection. Another bias is the clear–sky TOA incoming shortwave radiation. The simulated value is a few W/m^2 larger than observed for both the global mean and the warm–pool mean. This is mainly because of the surface albedo inaccurately prescribed in the model. It should be pointed out that when we developed the model we tried to simulate well both the global means of the above quantities and their geographical distributions. It can be seen from Table A–3 that even though the simulated all–sky TOA net incoming solar radiation over the warm pool is much smaller than observed, the global–mean value matches the observed very well as a result of cancellation of errors over the globe. This is also true for other all–sky quantities. A similar cancellation of errors was also found by Wild *et al.* (1995) when they compared radiative fluxes simulated by three versions of ECHAM GCMs and a few other GCMs with observations. Wild *et al.* (1995) mainly focused on the surface radiative fluxes.

b. Atmospheric Temperature and Zonal Wind
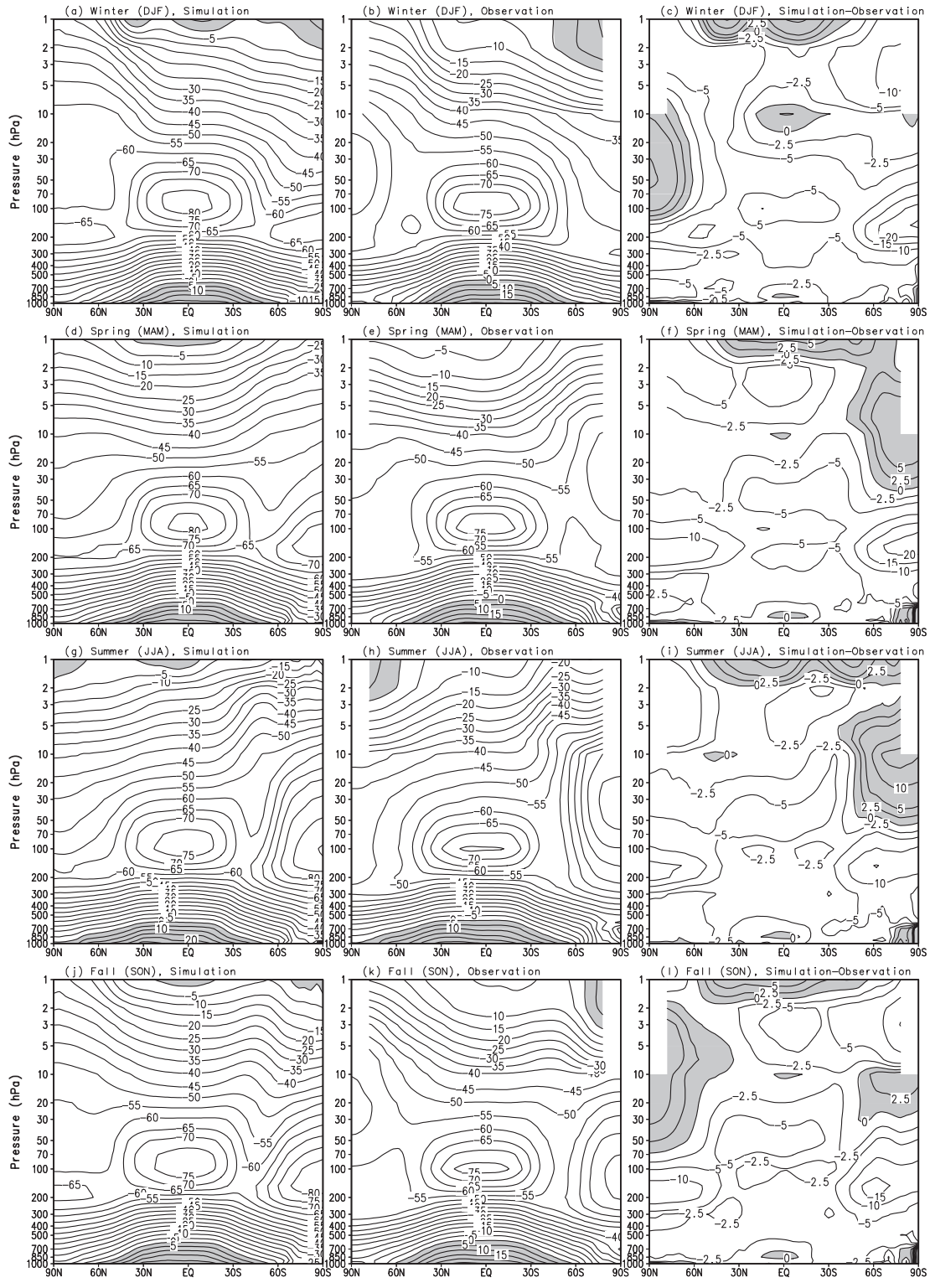
(1) Zonal–mean temperature

Latitude–height cross–sections of the simulated seasonal–mean zonal–mean temperature are presented in Fig. A–13 for the four seasons of the year, together with the corresponding observations and the differences between the simulated and the observed zonal–mean temperatures. Below 10 hPa the observed temperatures are the averages of the NCEP/NCAR Reanalysis from

1979 through 1995. Above 10 hPa the observed temperatures are from the COSPAR International Reference Atmosphere 1986 (CIRA–86) (Rees *et al.* 1990).

In all four seasons the model simulates well the temperatures in the troposphere and stratosphere everywhere except in the polar stratosphere. Temperature differences are less than 2.5°C in the troposphere and less than 5°C in the stratosphere in middle and low latitudes. The locations of the tropical tropopause and mid–latitude temperature gradients in the troposphere are well simulated. In the stratosphere, the model captures the opposite distributions of the pole–to–pole temperature gradient in JJA and DJF, and the reversals of the temperature gradient in MAM and SON.

The model is generally colder than observed, except in the middle polar stratosphere during polar night and near the stratopause. Swinbank *et al.* (1998) found a similar systematic cold bias in the UKMO Unified Model. They attributed that bias primarily to an inaccurately simulated longwave cooling rate. The bias in the UIUC 24–layer ST–GCM occurs for a different reason. The longwave radiation scheme of the 24–layer ST–GCM can produce clear–sky cooling rates with errors less than 0.4°C/day from the earth's surface up to 0.01 hPa when compared with line–by–line calculations (Chou and Suarez, 1994). Table A–3 shows that the simulated global–mean clear–sky TOA OLR and the simulated mean clear–sky TOA OLR over the warm pool match the ERBE satellite observations very well. The simulated clear–sky TOA net incoming solar radiation also matches the ERBE satellite observation reasonably well. The cold bias in the 24–layer ST–GCM is probably caused by an inaccurate radiative–transfer calculation in the cloudy atmosphere. Cloud distribution, cloud optical properties and the assumed cloud overlap in the model influence the simulated radiative heating and cooling of the atmosphere by clouds. The model has a smaller LW CRF and a larger SW CRF than the ERBE satellite observations. In the tropics the simulated absorption of solar radiation by clouds is substantially smaller than observed, especially over the warm pool (Table A–3). These errors lead to an overall larger–than–observed cooling effect by clouds. The cold bias in the troposphere in turn leads to a colder–than–observed lower and middle stratosphere because less longwave radiation is intercepted by the stratospheric atmosphere.

Fig. A–13. Latitude–altitude distributions of zonal–mean temperature for winter (DJF), spring (MAM), summer (JJA) and fall (SON), simulated (left–hand panels), observed (middle panels), and the differences between the simulated and observed (right–hand panels). Temperatures above 0°C and positive differences are shaded. The observed temperatures below 10 hPa are from the NCEP/NCAR Reanalysis, averaged from 1979 through 1995, and above 10 hPa from the COSPAR International Reference Atmosphere 1986 (CIRA–86) (Rees et al. 1990).

(a) Winter (DJF), Simulation (b) Winter (DJF), Observation (c) Winter (DJF), Simulation−Observation

(d) Spring (MAM), Simulation (e) Spring (MAM), Observation (f) Spring (MAM), Simulation−Observation

(g) Summer (JJA), Simulation (h) Summer (JJA), Observation (i) Summer (JJA), Simulation−Observation

(j) Fall (SON), Simulation (k) Fall (SON), Observation (l) Fall (SON), Simulation−Observation

Near its top the model is 5–10 ℃ warmer than observed because of a momentum damping (Hansen *et al.* 1983) applied to the model's top layer, the "sponge layer". This sponge layer absorbs vertically propagating waves forced from below and allows a large time–step to be used for the numerical integration of the model's dynamical processes which keeps the model from suffering computational instability.

In all seasons the model is about 10°C colder than observed in the lower polar stratosphere in the Northern Hemisphere and about 15°C to 20°C colder in the lower polar stratosphere in the Southern Hemisphere. These cold biases are common to many other GCMs. In SON and DJF, the model is about 6°C to 10°C warmer than observed in the middle and upper polar stratosphere in the Northern Hemisphere. In MAM and JJA, the model is about 6°C to 15°C warmer than observed in the upper polar stratosphere in the Southern Hemisphere. These warm biases do not exist in most other GCMs. Usually, systematic cold biases exist throughout the model atmosphere in the polar–night region, with a larger bias appearing in the upper stratosphere near 10 hPa (e.g., Hamilton *et al.* 1995). However, the Berlin Troposphere–Stratosphere–Mesosphere (TSM) GCM has a warm bias similar to that of the UIUC 24–layer ST–GCM in the polar stratospheres. Langematz and Pawson (1997) found that the Berlin TSM–GCM simulates temperature higher than observed in the polar region in the Northern Hemisphere in DJF. Near 30 hPa the bias is as much as 10°C. However, cold biases similar to those in most other GCMs exist in the Berlin TSM–GCM in the southern–hemisphere polar region in JJA. Langematz and Pawson (1997) attributed the warm bias primarily to the inaccurately simulated radiative heating, which may result from a cooling–to–space approximation for longwave radiative transfer above 20 hPa. Pawson *et al.* (1999) found that changing the strength of Rayleigh friction and the number of model layers to which Rayleigh friction was applied makes the Berlin TSM–GCM produce very different temperature structures near the North Pole. Rayleigh friction is used in the uppermost model layers of the Berlin TSM–GCM in the mesosphere to represent the unresolved subgrid–scale gravity–wave drag. No other gravity–wave–drag parameterizations are used. Langematz and Pawson (1997) found that increasing the number of layers to which Rayleigh friction is applied leads to an increase

of temperature by 13°C at 30 hPa. For the UIUC 24–layer ST–GCM, the warm bias exists in the middle and upper polar stratosphere in both hemispheres. As shown by the sensitivity studies in Section 2, the warm bias in the Northern Hemisphere is caused by the use of the Palmer *et al.* (1986) GWD parameterization. Without the parameterization, a cold bias prevails. The warm bias in the Southern Hemisphere is caused by the simulated larger–than–observed intensity of air–mass sinking in JJA (Rozanov *et al.* 1999a,b).

(2)   Zonal–mean zonal wind

Latitude–height cross–sections of the simulated seasonal–mean zonal–mean zonal wind are presented in Fig. A–14. In the troposphere, the model simulates well the locations and strengths of the sub–tropical jets in both hemispheres during all seasons, especially in the Northern Hemisphere. Similar to observations, the simulated northern–hemisphere tropospheric jet is much stronger in DJF than in JJA. The differences between the simulated and the observed zonal–mean winds are generally less than 5 m/s in the troposphere. In the stratosphere in all seasons except DJF, the simulated westerly and easterly winds have the observed strengths and positions. The transitions of westerly and easterly winds are captured. The tropospheric jets are well separated from the stratospheric polar–night jets in both boreal and austral winter. The simulation is better in the troposphere than in the stratosphere, and in MAM and JJA than in SON and DJF. Uniquely the 24–layer ST–GCM simulates the observed equatorward tilt of the southern polar–night jet core in JJA. Most current other GCMs do not simulate the tilt of this jet well.

One deficiency of the model is that the simulated northern polar–night jet is too weak in the middle stratosphere, and the jet core is shifted equatorward of its observed position. The observed equatorward tilt of the northern polar–night jet core from the polar tropopause to the mid–latitude stratopause is not properly simulated. The southern polar–night jet is also slightly weaker than observed. Most other GCMs simulate too–strong polar–night jets. The reason is that the 24–layer ST–GCM has warmer temperature in the middle–to–upper polar stratosphere than other GCMs. There are also some other minor discrepancies between the simulated and observed zonal winds. In DJF, the tropospheric subtropical jet in the Southern Hemisphere extends too high, up to 10 hPa, in
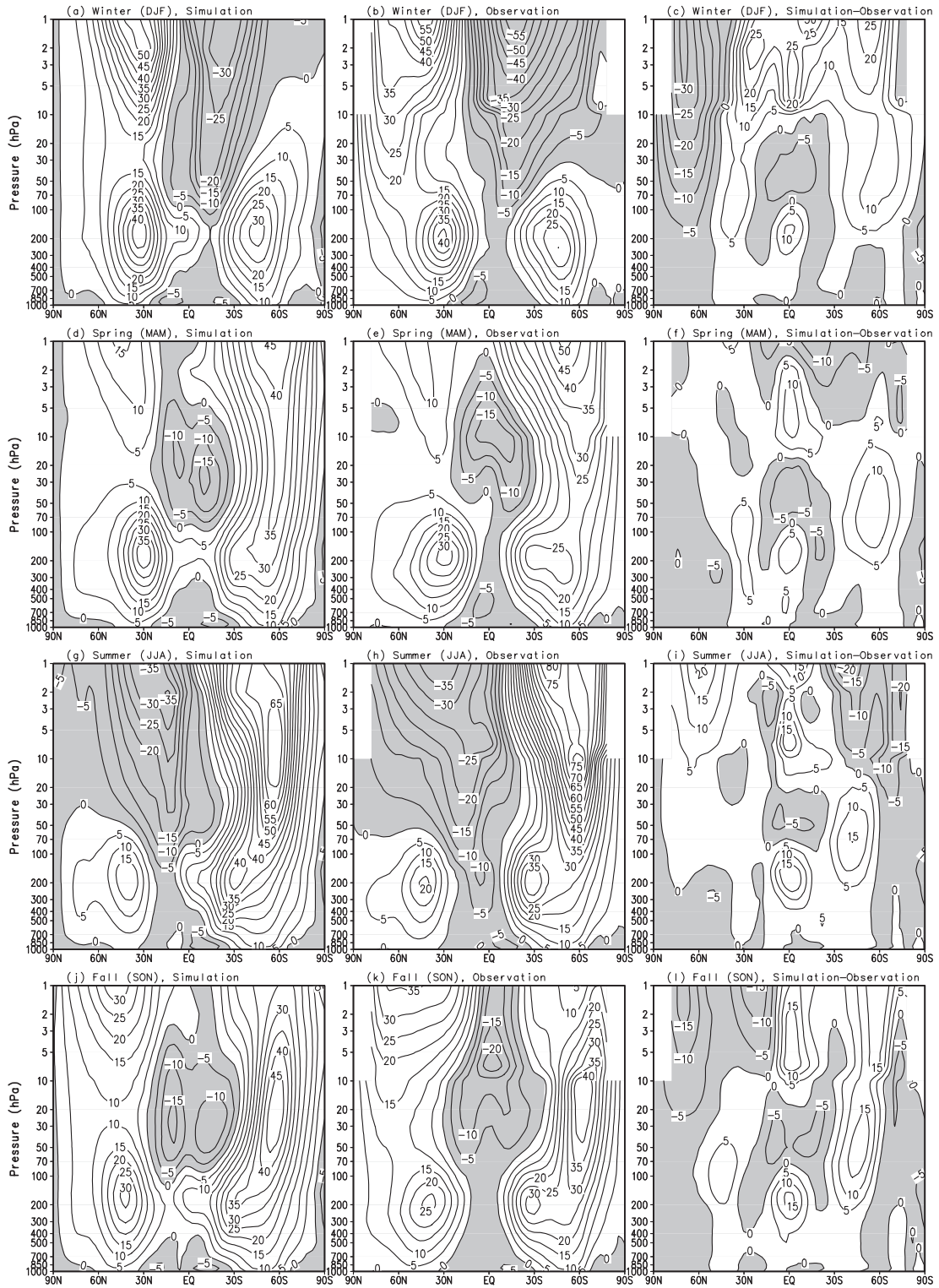
Fig. A–14. *As in Fig. A–13, except for zonal–mean zonal wind. Westerly wind and negative differences are shaded.*

contrast to the observed transition from westerly wind to easterly wind at about 50 hPa. This occurs via the thermal wind relation because the southern lower polar stratosphere is more than 20°C colder than observed in DJF. Near the tropical tropopause in MAM and SON, the simulated winds are westerly, but the observed winds are easterly. Also, the simulated strength of the stratospheric equatorial wind does not match the observed very well above 10 hPa.

(3)   Seasonal evolution of zonal wind at 10 hPa, 60°N and 60°S

The 24–layer ST–GCM has been coupled in an off–line mode, and will be coupled interactively, with a chemistry–transport model (Rozanov *et al.* 1999a,b) to simulate and understand the influence of interactive ozone photochemistry on greenhouse–gas–induced climate change, and the influence of greenhouse–gas–induced climate change on ozone, including the distribution of ultraviolet radiation at the earth's surface. The transitions of stratospheric winds from easterly to westerly and from westerly to easterly, and the breakdowns of the polar vortices are important for the transport of trace gases and chemical processes within the polar regions. The simulated and observed mean annual marches of monthly mean zonal–mean zonal wind at 10 hPa are presented in Fig. A–15. In the Northern Hemisphere the model simulates well the transitions from westerly to easterly in May and from easterly to westerly in September. But the simulated westerly jet core is located at 30°N, which does not correspond to the observed position at 60°N. In the Southern Hemisphere the meridional extent, the strength and seasonal variation of the polar vortex are well simulated. The strongest vortex appears in August and September. One shortcoming is that the simulated polar vortex does not break down at 60°S southward in DJF; however, further examination shows that it does break down in five out of the 12 simulated years (not shown). This indicates that the simulated southern polar stratospheric wind has a rather large interannual variability. It is also noticed from Fig. A–15 that the simulated north–south shift of the maximum easterly wind and its strength in the tropics are rather realistic.

To further explore the annual cycle and interannual variability of the polar stratospheric vortices in both hemispheres, we present in Fig. A–16 the simulated and observed mean annual march of monthly mean zonal–mean zonal wind at 60°S and 60°N, respectively. The time axis runs

from January to December at 60°S and from July to June at 60°N. At 60°S the simulated seasonal variation and strength of the zonal wind match the observed fairly well. In both the simulation and observation the strongest westerly wind is established in the upper stratosphere in April and May, intensifies progressively at lower levels and reaches its maximum near 10 hPa in August and September; and further propagates downward to the lower stratosphere until November with a gradually weakening strength. The simulated strong vortex in the upper stratosphere in August and September is in good agreement with the observations. The local maximum near 10 hPa matches the observed, though a little weaker. Most other current middle–atmosphere GCMs tend to largely overestimate the vortex here (e.g., Boville 1995; Manzini and Bengtsson 1996; Swinbank *et al.* 1998). However, in the upper stratosphere the simulated westerly wind is established in February, one month earlier than observed, and breaks down in November, one month later than observed. It is also noticed that in the lower stratosphere in March and April the simulated westerly wind is about 10 m/s larger than observed as a result of a colder–than–observed lower polar stratosphere. At 60°N, the model simulates the polar vortex poorly. The westerly wind decays too early in October and does not intensify and propagate further downward as does the observed. This deficiency is caused by the GWD parameterization in the model as described in previous sections.
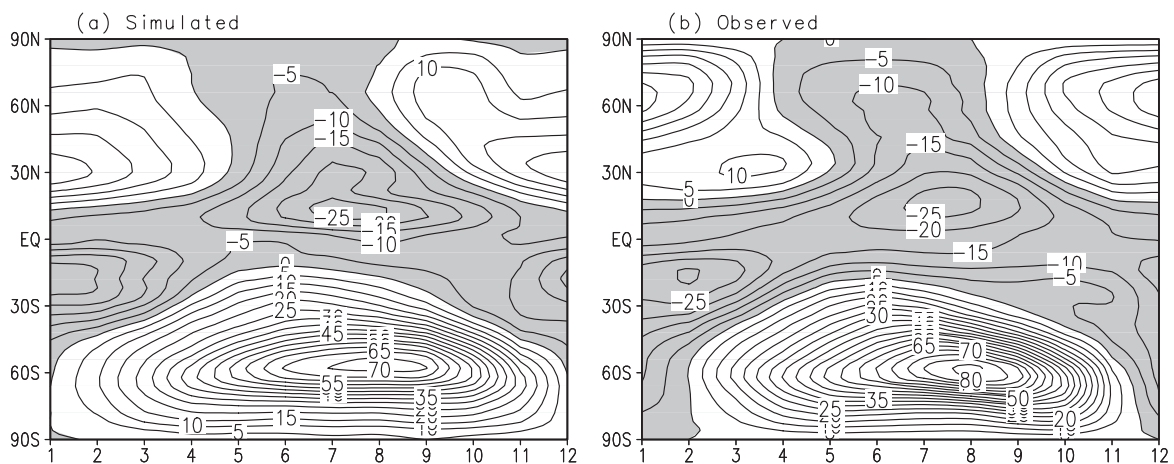

Fig. A–15.   *Mean annual march of zonal–mean zonal wind at 10 hPa from January to December for (a) the simulated and (b) the observed. Easterly winds are shaded.*
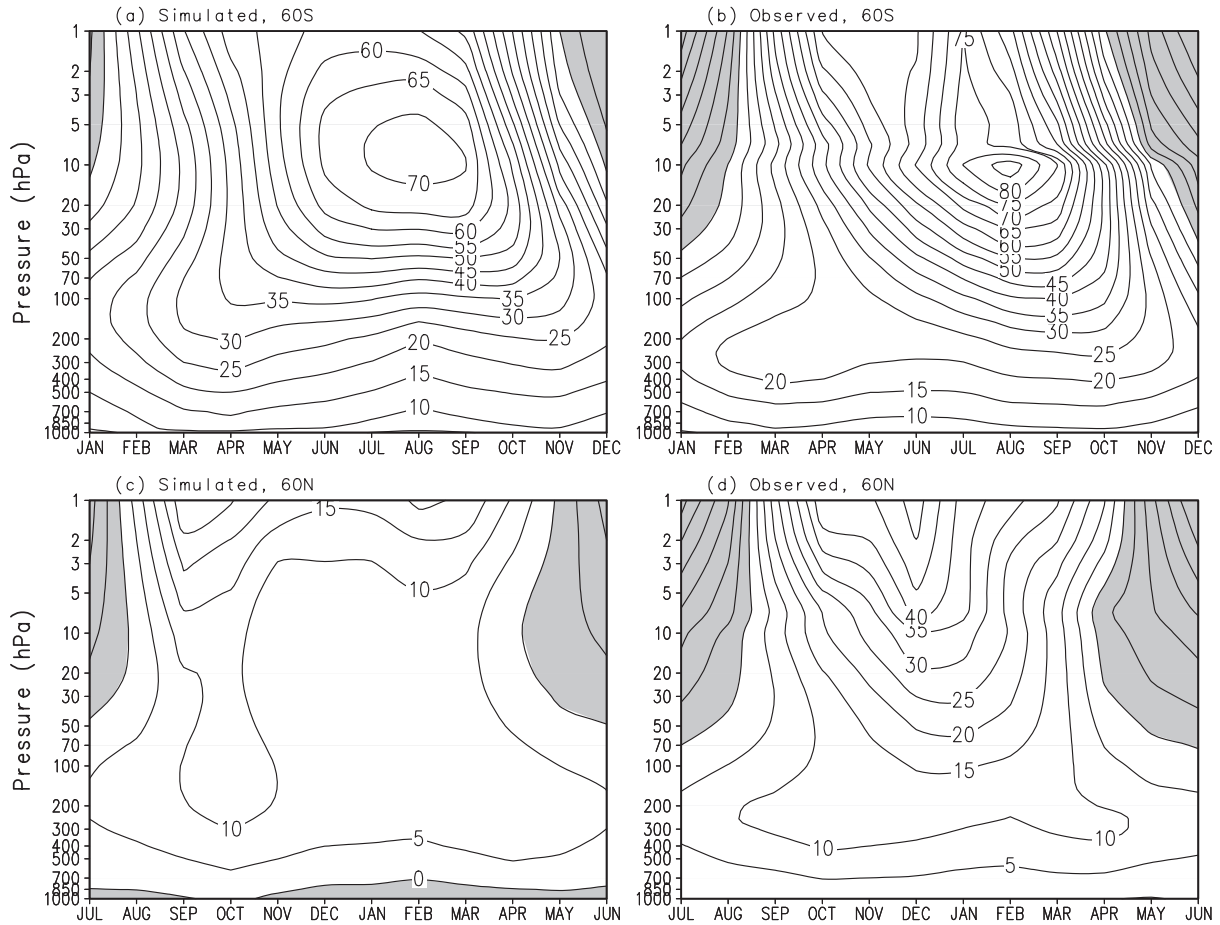
Fig. A–16. *Mean annual march of monthly mean zonal–mean zonal wind for the simulated at (a) 60°S and (c) 60°N, and the observed at (b) 60°S and (d) 60°N. The time axis runs from January to December at 60°S and from July to June at 60°N. Easterly winds are shaded.*

(4) Sudden stratospheric warming

The simulation of spontaneous sudden warmings in the polar stratosphere by a GCM is an important test of its capabilities. Many GCMs have succeeded in varying degrees in generating sudden stratospheric warmings, such as the UKMO Unified Model (Swinbank *et al.* 1998), the Canadian MAM (Beagley *et al.* 1997), and the ECHAM3.5 GCM (Manzini and Bengtsson 1996). We present in Fig. A–17 the variations of temperature at 10 hPa at the North Pole and South Pole

during the last three years of the simulation, sampled at 6–hour intervals. Each curve represents one simulated year. No sudden warmings exist at the South Pole, as in the real atmosphere. The model does show considerable variability at the North Pole from October through March. Multiple sudden warmings occur at the North Pole. Manzini and Bengtsson (1996) showed that the observed north–pole sudden stratospheric warmings usually begin in January and end in April. Here the simulated warmings begin in October and end in March. The model presents a larger variability than the real atmosphere at the North Pole from October to December. Such overestimated early–winter variability has also been found in other GCMs, namely, the UKMO Unified Model (Swinbank *et al.* 1998) and the Canadian MAM (Beagley *et al.* 1997).

To further illustrate the relation between the simulated sudden warmings and the zonal wind near the poles, we present in Fig. A–18 the time–latitude distributions of zonal–mean temperature and zonal wind at 10 hPa, sampled at 6–hour intervals for the three model years. A 13–point (~ 3 day) running–mean smoothing has been applied to the data before plotting. From about 60°N to the North Pole, synoptic–scale variations of temperature occur frequently from late October to late March in all three years. Polar–night jets break down and easterly winds build near the North Pole occasionally. In their comparison of sudden warmings simulated by the ECHAM3.5 GCM with observations, Manzini and Bengtsson (1996) used the following criteria in selecting major and minor sudden warming events: (1) a minor warming day requires that the meridional temperature gradient at 10 hPa between the North Pole and 60°N be positive, and (2) a major warming day requires not only a positive temperature gradient but also easterly winds at 60°N. A warming event must last at least four days. They found from a 15–year NMC–CAC analysis that almost no warmings exist before January; minor warmings occur at the highest frequency of days in March (35.9%), and major warmings in April (24%). Usually, the breakdown of the polar–night vortex follows the last major warming. Fig. A–18 shows that the 24–layer ST–GCM generates too many warmings, especially in early winter. Consequently, the modeled northern polar–night vortex is weaker and the seasonal–mean temperature is about 5°C to 10°C warmer than observed (see Fig. A–13). The westerly winds start to decay in early winter and do not intensify and propagate further

downward (see Fig. A–16). This deficiency is related to the GWD parameterization in the model. In the Southern Hemisphere the model simulates rather realistically the variations of temperature and zonal wind.
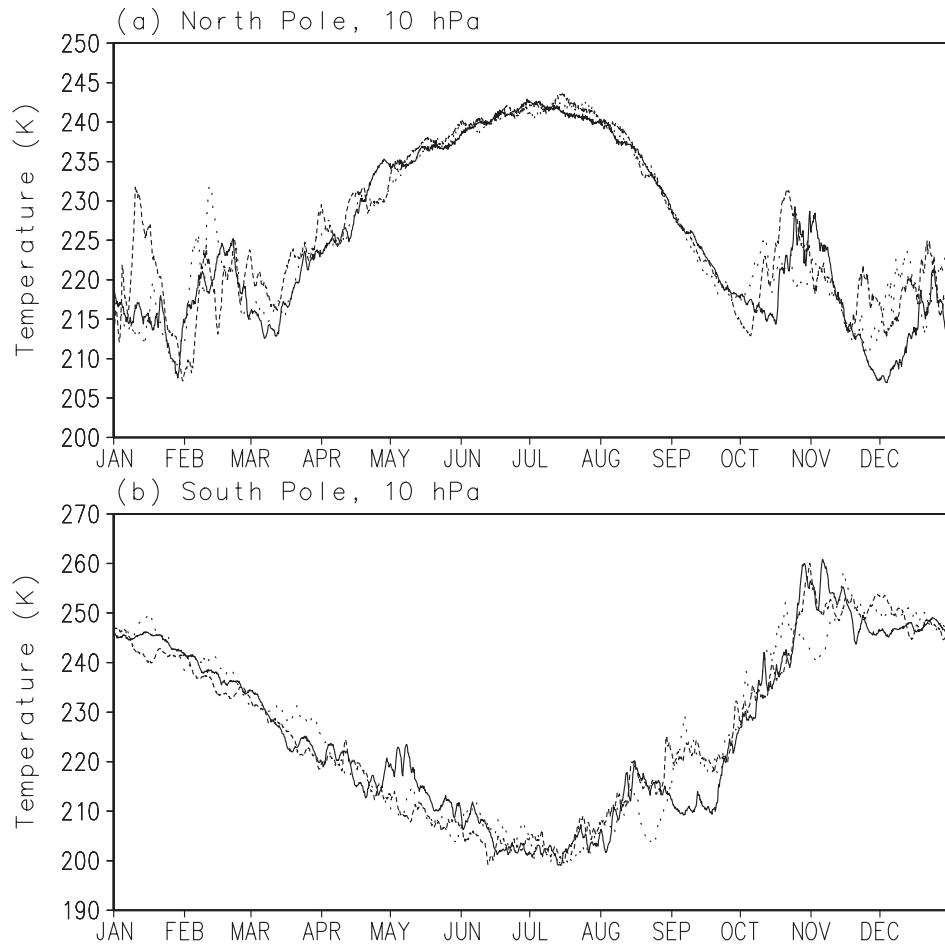

Fig. A–17. *Temperatures at 10 hPa at the North Pole and South Pole sampled at 6–hour intervals for three simulated years. Each curve represents one year of simulation.*
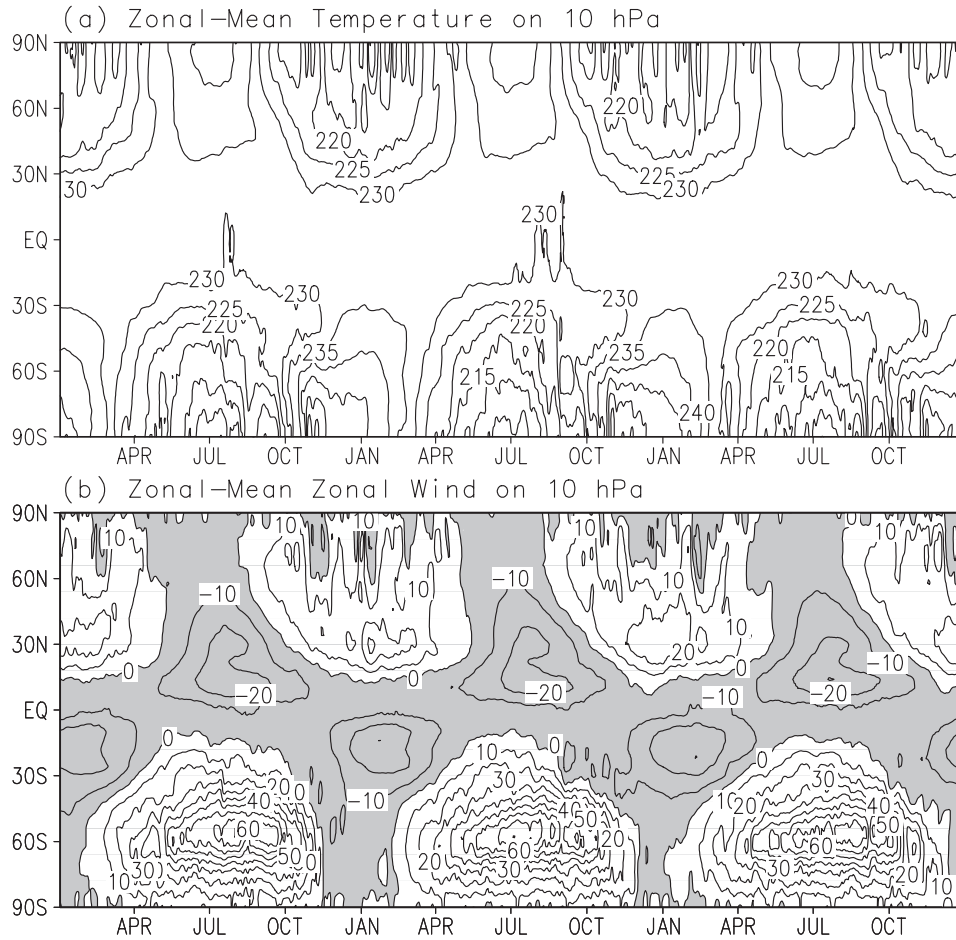
Fig. A–18. *Time–latitude distributions of the simulated zonal–mean temperature (a) and zonal wind (b) at 10 hPa sampled at 6–hour intervals for three simulated years. Before plotting, a 13–point filtering (~3 days) has been applied. Easterly winds are shaded.*

(5)   Equatorial zonal wind

The quasi–biennial oscillation (QBO) and the semi–annual oscillation (SAO) are the most intriguing features of the observed tropical atmospheric circulation. While most GCMs show the ability to simulate the SAO, it is still a great challenge for GCMs to capture even such basic features of the QBO as its amplitude, period, and vertical structure. Takahashi and Shiobara (1995) and Hamilton *et al.* (1995) reported some recent success in simulating the QBO using simplified GCMs. Takahashi and Shiobara (1995) simulated the long–period and large–amplitude equatorial zonal–mean wind oscillations using a spectral model with high horizontal resolution (triangular truncation 106). The model is highly simplified. It has an ocean–only surface with prescribed zonally homogeneous surface temperature. The boundary layer has no zonal variation and interhemispheric asymmetry. The model was forced with annual–mean radiation. Therefore, the annual cycle and quasi–stationary waves were not included. Hamilton *et al.* (1995) integrated the GFDL SKYHI model with 3° resolution in latitude for 64 months with no topography and with the solar declination and SSTs frozen at their March 21 values.   A QBO–like oscillation in the tropics was obtained. It had a downward phase propagation and long period, but an amplitude only about 15 m/s and centers at the 1.5 hPa level, much higher than the observed center. Most recently, Takahashi (1999) reported the simulation of a more realistic QBO in a high–vertical–resolution model (60 layers) with reduced damping of the smallest–scale (gravity) waves.

Fig. A–19 shows the march of the simulated monthly mean zonal–mean zonal wind at the equator in the stratosphere for five simulated years by the UIUC 24–layer ST–GCM. The SAO near the stratopause is fairly realistic. The easterly wind has its first maximum in January near 1 hPa and its second maximum in July at a lower altitude near 3 hPa. The westerly wind has maxima in April and October, centered at 2 hPa.   Both the easterly and westerly phases have prominent downward–phase propagation similar to the observations. Given the model top at 1 hPa and the momentum damping applied to the topmost model layer, the oscillation seems to be centered at a little lower altitude than observed and its strength is also weaker. Not surprisingly, the UIUC 24–layer ST–GCM did not succeed in simulating the QBO, most likely because the model's

horizontal and vertical resolutions are too coarse to simulate well the vertical momentum transport by small–scale gravity waves.
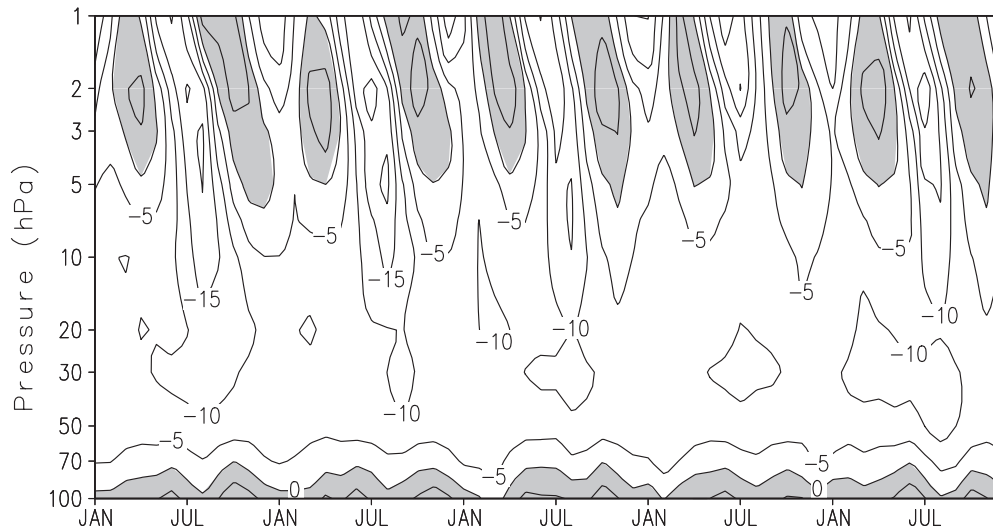

Fig. ***A–19***. *March of the simulated monthly mean zonal–mean zonal wind at the equator for five simulated years. Westerly winds are shaded. The contour interval is 5 m/s.*

c. Residual Circulation and Eliassen–Palm Flux Divergence

To diagnose the simulated mean–meridional circulation from a Lagrangian point of view and the interactions between the zonal–mean zonal wind and eddy disturbances, we present the simulated residual meridional and vertical winds from the framework of the Transformed Eulerian Mean (TEM) circulation in the stratosphere (Andrews and McIntyre 1976), together with a diagnosis of the zonal momentum tendency in terms of the divergence of the Eliassen–Palm (EP) flux. For two reasons the analysis was performed only for the stratosphere. First, the integration of the model is performed for sigma (σ) layers and the model outputs are transformed onto standard isobaric (p) surfaces. Interpolation of variables, especially eddy fluxes, from σ–layers to p–surfaces might introduce large errors in the troposphere because these two coordinate surfaces often cross each other with large angles in the troposphere. Second, we saved only the temperature and its product

with the winds during the model integration. To perform the TEM calculation, we need to convert temperature and the meridional temperature flux into potential temperature and the meridional potential temperature flux. In the troposphere isothermal and isentropic surfaces have almost opposite slopes, especially in the mid–latitudes. Using temperature and the meridional temperature flux on isobaric surfaces to produce potential temperature and the meridional potential temperature flux by simply multiplying them by $(p_o/p)^\kappa$ would introduce large errors, especially for the eddy fluxes. In the stratosphere, the above problems do not occur because the σ and isobaric surfaces are almost parallel to each other and isentropic surfaces are almost parallel to isobaric surfaces.

We performed our analysis using eddy fluxes of momentum and potential temperature sampled at 6–hour intervals and the monthly means of other quantities on the 22 isobaric surfaces of the standard model output (1000, 925, 850, 700, 600, 500, 400, 300, 250, 200, 150, 100, 70, 50, 30, 20, 10, 7, 5, 3, 2, and 1 hPa). For each of the 12 simulated years, the monthly mean residual circulation and EP–flux divergence were derived. Then ensemble seasonal means averaged over the 12 simulated years were calculated. Latitude–height cross–sections of the ensemble residual meridional velocity $[\overline{v}]_r$ and residual vertical velocity $[\overline{w}]_r$ for the DJF and JJA seasons are presented in Fig. A–20, together with the mass streamfunction of the residual circulation. An approximation, $[\overline{\omega}]_r = -[\overline{\rho}]g[\overline{w}]_r$, has been used to convert the vertical velocity $[\overline{\omega}]_r$ in Pascal/s in p–coordinate to $[\overline{w}]_r$ in cm/s in z–coordinate, where $[\overline{\rho}]$ is the monthly mean zonal–mean air density. The mass streamfunction of the residual circulation is calculated by integrating $[\overline{v}]_r = \dfrac{g}{2\pi R_e \cos\phi} \dfrac{\partial \psi}{\partial p}$ from the top of the model, where $\psi = 0$, to 100 hPa. Positive values indicate clockwise motion. We set the North Pole on the right–hand side in Fig. A–20, contrary to the convention of the other figures in this appendix, to compare with published results.

We compare the simulated residual meridional and vertical velocities with those in Figs. A–6 and 7 of Coy and Swinbank (1997) who used the stratospheric data–assimilation systems of the Goddard Space Flight Center (GSFC) and the U.K. Meteorological Office (UKMO). It should be
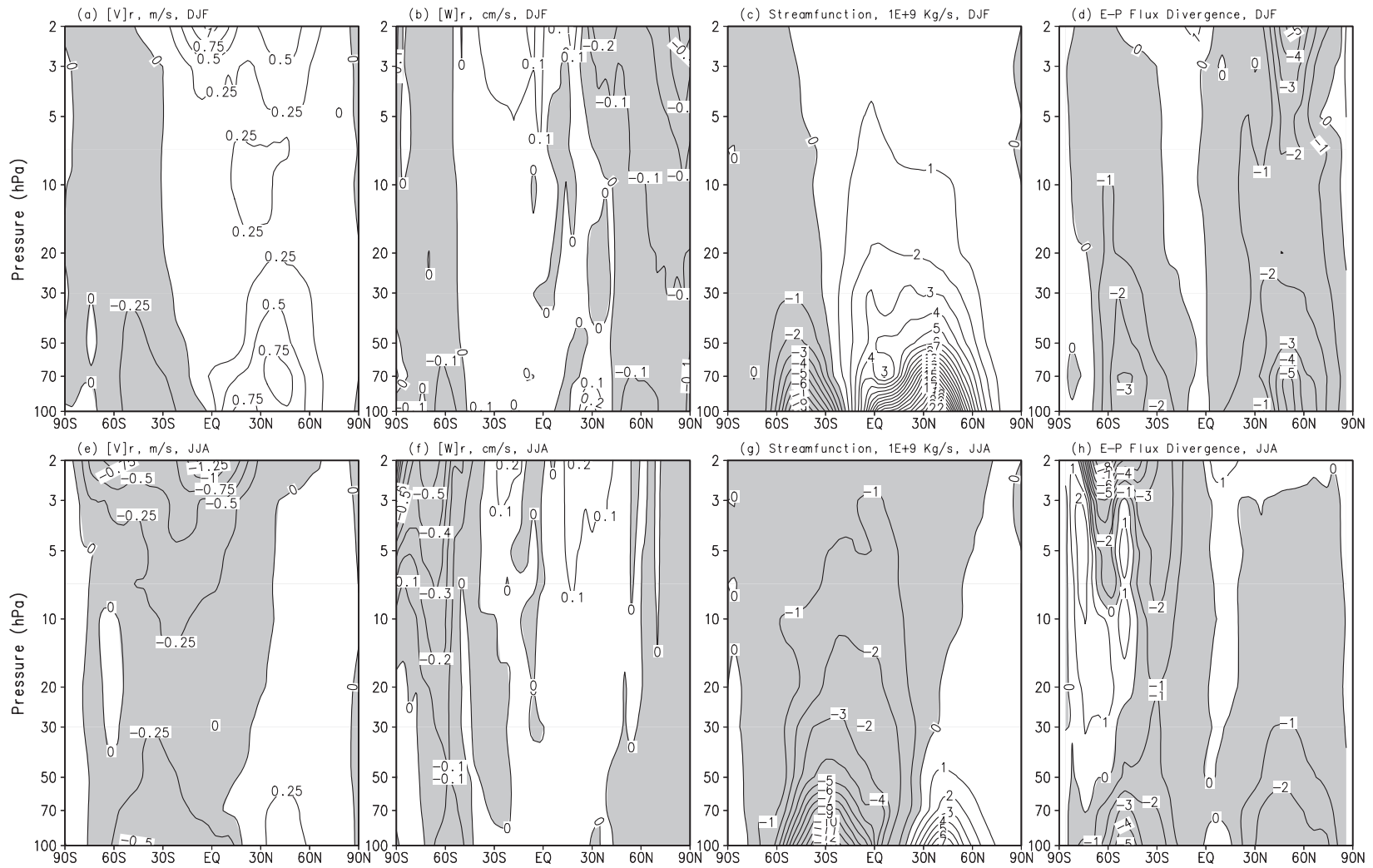
Fig. A–20.   *Ensemble residual meridional velocity (m/s) in (a) and (e), residual vertical velocity (cm/s) in (b) and (f), mass streamfunction of the residual circulation (10⁹ kg/s) in (c) and (g), and forcing of zonal–mean zonal wind by the model–resolved eddies in terms of the E–P flux divergence (ms⁻¹/day) in (d) and (h). The upper panels are for DJF and the lower panels are for JJA. Negative values are shaded.*

noted that: (1) the model configurations are different among the UIUC 24–layer ST–GCM and the two assimilation systems used by Coy and Swinbank (1997); (2) Coy and Swinbank (1997) presented the residual circulation only for 1992, while we present here a 12–year average; (3) the UKMO and GSFC assimilation systems used different insertion methods for the observed data; and (4) the UKMO assimilation ran once per day, while the GSFC assimilation ran at 6–hour intervals. The diagnosis of model output here is based on 6–hourly sampling. Since the calculations of the residual circulation are based on eddy fluxes, these differences might affect the comparability. Therefore, the following comparison is only qualitative.

In the stratosphere, in comparison with the two assimilations, the UIUC 24–layer ST–GCM reproduces well the two–cell Brewer–Dobson circulation in both DJF and JJA, that is, one stronger branch of motion toward the winter pole and another weaker branch of motion toward the summer pole. The observed seasonal reversal of the pole–to–pole circulation near the stratopause is simulated. The simulated $[\overline{v}]_r$ resembles more closely the GSFC assimilation than the UKMO assimilation. Near the stratopause in each season, a primary maximum of the residual meridional velocity $[\overline{v}]_r$ of about 1.0 m/s appears in the tropics, and a secondary maximum appears in the high latitudes in the winter hemisphere. The UKMO assimilation produces the strongest $[\overline{v}]_r$, and the maxima of $[\overline{v}]_r$ in the winter hemisphere near the stratopause are closer to the poles than are those of the GSFC assimilation and the UIUC 24–layer ST–GCM. One noticeable difference between these two assimilations is the near–pole "breaks" of mass transport. In the middle stratosphere the GSFC assimilation produces a weak northward transport in the high latitudes of the Southern Hemisphere and a southward transport in the high latitudes of the Northern Hemisphere. The UKMO assimilation does not have these transports. Figs. A–20 (a) and (e) show that the UIUC 24–layer ST–GCM simulates rather weak "breaks".

Coy and Swinbank (1997) derived the residual vertical velocity $[\overline{w}]_r$ indirectly using $[\overline{v}]_r$ based on the TEM mass continuity equation. We calculated $[\overline{w}]_r$ directly from the vertical velocity and the eddy flux of potential temperature. The diagnosed $[\overline{w}]_r$ agrees with the two assimilations in

general, with ascending motion in the summer hemisphere and descending motion in the winter hemisphere. Their magnitudes are also comparable.

To understand the contribution of the "model–resolved" eddy disturbances to the maintenance of zonal–mean zonal wind, we diagnosed the Eliassen–Palm (EP) flux divergences (ms^{-1}/day) and present them in Figs. A–20 (d) and (h). Both stationary eddies and transient eddies are included in the EP–flux divergences. In the middle to upper stratosphere in both DJF and JJA, strong easterly forcing exists in the winter–hemisphere high latitudes, very weak easterly forcing in the summer hemisphere, and weak westerly forcing in the tropics and polar–night regions. The magnitude of the forcing in the upper stratosphere matches those simulated by the two mesospheric GCMs, the MACCM2 T42xL21 (Boville 1995) and the Berlin TSM–GCM (Langematz and Pawson 1997). In the lower stratosphere, in comparison with those two mesospheric GCMs, the UIUC 24–layer ST–GCM seems to generate stronger easterly forcing in both hemispheres in DJF and JJA.

4. Test of Rayleigh Friction and GWD in a Mesosphere Model

In Section 3 a warm bias was found in the UIUC 24–layer ST–GCM, similar to the one in the Berlin TSM–GCM (Langematz and Pawson 1997), in the northern middle to upper polar stratosphere in DJF. The bias in the UIUC 24–layer ST–GCM is due to the GWD parameterization, but the bias in the Berlin TSM–GCM is most likely due to an inaccurate longwave radiation scheme. The orographic–type GWD parameterization used in the UIUC model tends to warm the northern polar stratosphere. With increasing number of model layers in the mesosphere to which Rayleigh friction is applied, the Berlin TSM–GCM tends to simulate a cooler northern polar (Pawson *et al.* 1999). These opposite results suggest that a GCM using both the GWD parameterization and Rayleigh friction might be able to produce "correct" polar stratospheric temperature through a cancellation of opposing biases. A few mesosphere GCMs have included both the orographic–type GWD in the troposphere and lower stratosphere and Rayleigh friction in the upper stratosphere and mesosphere, namely, the NCAR Middle Atmosphere Version of CCM2 (Boville 1995), the

Canadian Climate Center's Middle Atmosphere Model (Beagley *et al.* 1997), and the UKMO Unified Model (Swinbank *et al.* 1998).

To test this idea we developed a 36–layer troposphere–stratosphere–mesosphere GCM with its top at 0.01 hPa based on the UIUC 24–layer ST–GCM. This model has 6 layers between 0.01 hPa and 1 hPa, 13 layers between 1 hPa and 100 hPa, and 17 layers below 100 hPa. In addition to the changes of the vertical resolution and the altitude of the model's top, Rayleigh friction (Boville 1986) was used above 10 hPa to replace the GWD parameterization of Palmer *et al.* (1986). The coefficient of Rayleigh friction was set to be $\{1 + \tanh[(z - 52)/7.5]/3\}$, where z is geopotential height in km. Other than these changes, the 36–layer TSM–GCM is identical to the 24–layer ST–GCM.

A 93–day perpetual–January simulation was performed using the 36–layer TSM–GCM. The model was initialized on 1 January by making use of available observations and initial fields of the 24–layer ST–GCM. The averages over the last 62 days of the simulated zonal–mean temperature and zonal wind are presented in Fig. A–21, together with the observations and the differences between the simulations and the observations. The warm bias in the northern middle to upper polar stratosphere in the 24–layer ST–GCM (Fig. A–13) becomes a –10°C to –15°C cold bias. The northern polar–night jet in the lower stratosphere between 100 hPa and 10 hPa becomes much stronger in the 36–layer TSM–GCM than in the 24–layer ST–GCM (Fig. A–14), and the jet core between these two isobaric surfaces has the observed position and is not shift to the mid–latitude as it is in the 24–layer ST–GCM simulation. However, the two poles in the lower stratosphere are too cold. The mesosphere is too warm. The observed equatorward tilt of the polar–night jet core in the Northern Hemisphere is not captured. These deficiencies are common to most other mesosphere GCMs, regardless of whether or not Rayleigh friction has been used in these GCMs to represent the effect of gravity–wave drag in the mesosphere (e.g., Beagley *et al.* 1997).

This experiment indicates that the interactions between the mesosphere and the stratosphere are important for simulations of the stratosphere. The use of both the orographic–type GWD and Rayleigh friction in a GCM needs further investigation. The fundamental problem of how to better

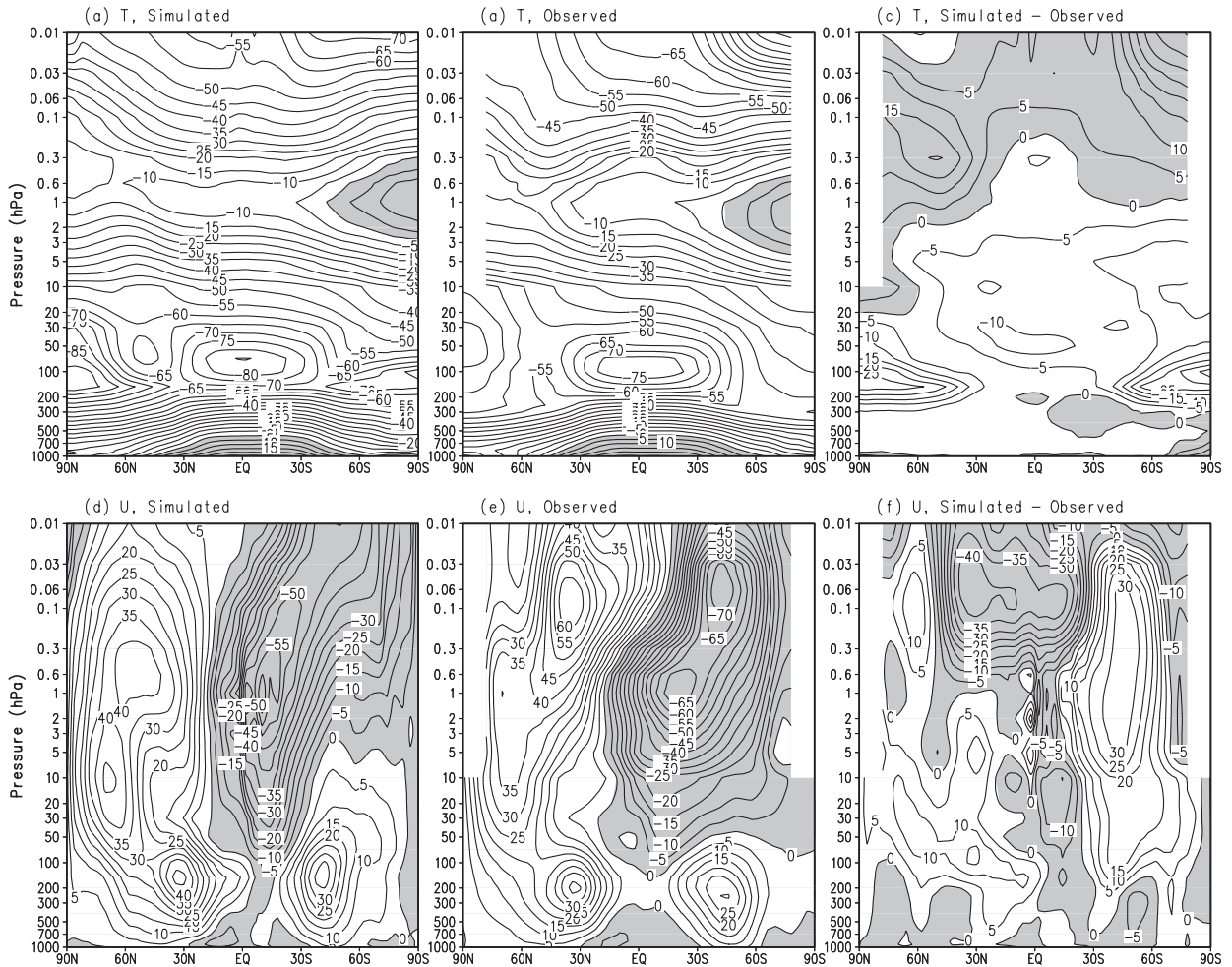parameterize subgrid–scale gravity waves in both the troposphere and middle atmosphere remains to be solved.

Fig. A–21. *Zonal–mean temperature and zonal wind for the simulated in (a) and (d) and the observed in (b) and (e), and the differences between the simulated and the observed in (c) and (f). The simulated temperatures and winds are the last 62–day averages from a 93–day perpetual–January simulation of the UIUC 36–layer TSM–GCM. Temperatures above 0°C and easterly winds are shaded. Positive differences for temperature and negative differences for zonal wind are also shaded.*

5. Summary and Discussion

In this appendix, we have introduced the UIUC 24–layer stratospheric–tropospheric general–circulation model. Compared to its ancestors, the model has a finer vertical resolution and extends higher, to the stratopause. New schemes were adopted and developed for the transfer of terrestrial and solar radiation, the interaction between clouds and radiation was revised, the radiative effect of aerosols in both the troposphere and stratosphere was included, and the Palmer *et al.* (1986) parameterization of orographically excited subgrid–scale gravity–wave drag was implemented with modifications. The new parameterization for terrestrial radiation takes into account the Doppler broadening of the absorption lines for water vapor, CO_2 and O_3 in the upper stratosphere. Calculations by column radiative–transfer models show that the new terrestrial radiation routine improves the cooling rates in both the troposphere and stratosphere, and the new solar radiation routine yields generally better heating rates in the upper stratosphere. The inclusion of the GWD parameterization improves the simulated tropospheric subtropical jets and sea–level pressure in both hemispheres; however, it weakens the polar–night jet in the Northern Hemisphere.

To validate the model, a 15–year control simulation was performed with climatological SST and sea–ice extent. The simulated geographical distributions and seasonal variations of surface–air temperature, precipitation, cloud cover, and cloud radiative forcing were compared with observations. The model simulates well the surface–air temperature over the globe, except near the poles. The observed geographical distribution of precipitation was simulated reasonably well. The seasonal variation of the heavy precipitation in the tropics associated with the ITCZ was captured. The simulated cloud cover generally matches the observed, except in the high latitudes of the Southern Hemisphere, where the simulated cloud cover is about 20% to 30% less than observed. It has been found that the scheme used to diagnose the large–scale fractional cloud (Sundqvist, 1978; 1988) in the model is very sensitive to relative humidity. The simulation of cloud cover in the high latitudes and near the poles was improved by modifying this scheme. The model simulates well the clear–sky TOA OLR and TOA net incoming solar radiation, except that it systematically underestimates the reflection of solar radiation over open–water surfaces because of the inaccuracy

of the prescribed surface albedo. Under cloudy sky, the model simulates well the observed geographical distribution and seasonal variation of the LW CRF, especially in the tropics. It is found that the LW CRF in the tropics largely depends on the height of convective clouds, which in turn depends on the threshold relative humidity that controls the onset of penetrating convection in the model (Wang and Schlesinger 1999). For the SW CRF, the model captured its observed geographical distribution and seasonal variation in general. The model overestimated the SW CRF in the tropics and subtropics and underestimated the SW CRF in high latitudes. The largest bias occurred near 60°S in January because of the inaccurately simulated cloud cover. Over the warm pool, the simulated absorption of solar radiation by clouds is 35 W/m^2 smaller than the ERBE satellite observation.

The simulated atmospheric temperature and circulation were also diagnosed. The model simulates well the observed position of the tropical tropopause, the tropospheric temperature gradients in the middle latitudes and the subtropical jet streams. In the stratosphere, the observed distributions of pole–to–pole temperature gradient in JJA and DJF are captured, and the polar–night jet in the Southern Hemisphere has its observed strength and position. The model also captured the location and phase of the observed semi–annual oscillation near the stratopause. Stratospheric sudden warmings were also simulated in the northern–middle stratosphere. However, a number of deficiencies exist. The model has a colder–than–observed lower polar stratosphere. In SON and DJF, the model is about 6°C to 10°C warmer than observed in the middle and upper polar stratosphere of the Northern Hemisphere. In MAM and JJA, the model is about 6°C to 15°C warmer than observed in the southern upper polar stratosphere. The simulated northern polar–night jet is too weak compared to observations and the jet core is shifted equatorward. The simulated southern polar vortex is also a little weaker than observed. The warm bias and the weak polar vortex in the Northern Hemisphere have not been observed in most other GCMs, which usually simulate systematic cold biases and over–intensified polar vortexes. Sensitivity studies in Section 2 indicate that the warm bias in the 24–layer ST–GCM is related to the use of the GWD parameterization.

The analysis of residual circulation indicates that the model simulates reasonably well the observed two–cell Brewer–Dobson circulation in the stratosphere and its reversal between the two solstice seasons. The model generates easterly forcing by the model–resolved eddies in the middle to upper stratosphere in winter hemispheres, comparable to those simulated by other mesospheric GCMs. However, the forcing in the lower stratosphere is too strong.

In this appendix attention has been paid to the warm bias in the polar–night regions and the weak circumpolar vortex in the middle–to–upper polar stratosphere of the Northern Hemisphere. It was found that these biases changed to their opposite directions in the 36–layer TSM–GCM, which uses a parameterized orographic–type GWD below 10 hPa and Rayleigh friction above 10 hPa.

In summary, the UIUC 24–layer ST–GCM has significantly improved the simulation in the troposphere and near the surface compared to its ancestors. It also simulates reasonably well the stratospheric temperature and circulation, except the northern polar–night jet. To further develop the model, special attention should be paid to the simulation of cloud cover and the parameterization of the subgrid–scale gravity–wave drag. The simulated radiative forcing and many tropospheric variables largely depend on the spatial distributions of cloudiness. A better GWD parameterization is expected to be able to significantly improve the simulation in the stratosphere.